Structure of Ca^{2+}-Bound S100A4 and Its Interaction with Peptides Derived from Nonmuscle Myosin-IIA†

Vladimir N. Malashkevich,‡,§ Kristen M. Varney,§,|| Sarah C. Garrett,‡,§ Paul T. Wilder,|| David Knight,‡,⊥ Thomas H. Charpentier,|| Udupi A. Ramagopal,‡ Steven C. Almo,*,‡ David J. Weber,*,|| and Anne R. Bresnick*,‡

Department of Biochemistry, Albert Einstein College of Medicine, 1300 Morris Park Avenue, Bronx, New York 10461, and Department of Biochemistry and Molecular Biology, University of Maryland School of Medicine, 108 North Greene Street, Baltimore, Maryland 21201

Received December 27, 2007; Revised Manuscript Received March 19, 2008

ABSTRACT: S100A4, also known as mts1, is a member of the S100 family of Ca^{2+}-binding proteins that is directly involved in tumor invasion and metastasis via interactions with specific protein targets, including nonmuscle myosin-IIA (MIIA). Human S100A4 binds two Ca^{2+} ions with the typical EF-hand exhibiting an affinity that is nearly 1 order of magnitude tighter than that of the pseudo-EF-hand. To examine how Ca^{2+} modifies the overall organization and structure of the protein, we determined the 1.7 Å crystal structure of the human Ca^{2+}-S100A4. Ca^{2+} binding induces a large reorientation of helix 3 in the typical EF-hand. This reorganization exposes a hydrophobic cleft that is comprised of residues from the hinge region, helix 3, and helix 4, which afford specific target recognition and binding. The Ca^{2+}-dependent conformational change is required for S100A4 to bind peptide sequences derived from the C-terminal portion of the MIIA rod with submicromolar affinity. In addition, the level of binding of Ca^{2+} to both EF-hands increases by 1 order of magnitude in the presence of MIIA. NMR spectroscopy studies demonstrate that following titration with a MIIA peptide, the largest chemical shift perturbations and exchange broadening effects occur for residues in the hydrophobic pocket of Ca^{2+}-S100A4. Most of these residues are not exposed in apo-S100A4 and explain the Ca^{2+} dependence of formation of the S100A4−MIIA complex. These studies provide the foundation for understanding S100A4 target recognition and may support the development of reagents that interfere with S100A4 function.

S100A4, also called mts1, is a member of the S100 family of small, homodimeric, EF-hand Ca^{2+} binding proteins. S100 proteins are expressed in a tissue specific manner and bind to a variety of target proteins, resulting in the regulation of specific cellular processes, including cell-cycle regulation, protein phosphorylation, cell growth, motility, differentiation, and survival (*1–4*). While S100A4 is expressed in a wide range of normal tissues (*5, 6*), it is recognized that an increased level of S100A4 expression correlates with a high incidence of metastasis and poor prognosis for cancer patients (*7, 8*). High S100A4 expression levels are associated with several metastatic cancers, including breast (*9*), colorectal (*10*), bladder (*11*), esophageal (*12*), non-small cell lung (*13*), gastric (*14*), medulloblastoma (*15*), pancreatic (*16*), prostate (*17*), and thyroid (*18*). In colorectal cancer, S100A4 is a direct transcriptional target of the β-catenin−T-cell factor (TCF) complex (*19*), a component of the Wnt/β-catenin pathway that is frequently unregulated as a result of mutations that affect the phosphorylation and stabilization of β-catenin (*20–22*). In medulloblastoma, enhanced S100A4 expression occurs via ErbB2 signaling and the PI3K/Akt and Erk 1/2 pathways (*15*). These findings suggest that multiple signaling cascades can lead to elevated S100A4 levels.

S100A4-induced metastasis observed in vivo is thought to result from S100A4-mediated increases in motility and invasion observed at the cellular level (*8, 19*). At the molecular level, S100A4 is recognized as a Ca^{2+}-activated switch (*8, 23*), which in the Ca^{2+}-loaded form adopts a conformation that allows it to bind target proteins. Cytoskeletal and signaling targets of S100A4 include nonmuscle myosin-IIA (*24, 25*), tropomyosin (*26*), F-actin (*27*), and liprin β1, an interacting protein of the LAR family of transmembrane tyrosine phosphatases (*28*).

The Ca^{2+}-dependent interaction of S100A4 with myosin-IIA prevents oligomerization and promotes the monomeric, unassembled state of myosin-IIA (*29*). This observation is consistent with data showing that the S100A4 binding site maps to the C-terminal end of the coiled coil of the myosin-IIA heavy chain (*29*) and that the S100A4 binding site overlaps the extended assembly competence domain, which is required for myosin-II assembly (*30, 31*). Furthermore, phosphorylation by casein kinase 2 on Ser1943 of the myosin-IIA heavy chain, which is downstream of the S100A4

† This work was supported by National Institutes of Health Grants GM069945 (A.R.B.), GM58888 (D.J.W.), and CA107331 (D.J.W.) and American Cancer Society Grant CDD107745 (D.J.W.).

* To whom correspondence should be addressed: A.R.B.: telephone, (718) 430-2741; fax, (718) 430-8565; e-mail, bresnick@aecom.yu.edu. D.J.W.: telephone, (410) 706-4354; fax, (410) 706-0458; e-mail, dweber@umaryland.edu. S.C.A.: telephone, (718) 430-2746; fax, (718) 430-8565; e-mail, almo@aecom.yu.edu.

‡ Albert Einstein College of Medicine.

§ These authors contributed equally to the completion of this work.

|| University of Maryland School of Medicine.

⊥ Current address: Department of Biology and Biochemistry, University of Bath, Bath BA2 7AY, U.K.

10.1021/bi702537s CCC: $40.75
Published on Web 04/15/2008

binding site, inhibits S100A4 binding and protects against S100A4-induced disassembly of myosin-IIA filaments (*29, 32*). Thus, heavy chain phosphorylation, as well as Ca^{2+} binding, regulates the S100A4−myosin-IIA interaction. In addition, S100A4 modulates the polarization and motility of carcinoma cells through a direct interaction with myosin-IIA (*33*). This interaction likely plays a role in the contribution of S100A4 to metastasis (*8*).

The interaction of S100A4 with myosin-IIA is strictly Ca^{2+}-dependent (*25, 29*). Similar to other S100 proteins, S100A4 is a symmetric homodimer with each subunit containing two EF-hand Ca^{2+}-binding loops: a C-terminal typical EF-hand and an N-terminal pseudo-EF-hand comprised of 14 residues (instead of 12). The apo-S100A4 consists of four helices and a small β-sheet with two helices from each subunit (1, 4, 1′, and 4′) forming a tight X-type four-helix bundle that comprises the dimer interface (*23*). When Ca^{2+} binds, helix 3 in each S100A4 subunit rotates by ~60° relative to helix 4 and exposes a hydrophobic cleft in a manner similar to that observed for other S100 proteins (*34–36*).

To further characterize the interaction between myosin-IIA and S100A4, we examined the binding of S100A4 to Ca^{2+} and peptides derived from the C-terminus of myosin-IIA. These data together with the X-ray structure of the Ca^{2+}-S100A4 have allowed us to map the surface on Ca^{2+}-activated S100A4 that interacts with myosin-IIA. Such information is necessary to understand the Ca^{2+} dependence of the S100A4−MIIA[1] interaction and could be useful for understanding how S100A4 depolymerizes highly stable myosin-IIA filaments. These results could also aid in the design of S100A4 inhibitors, some of which may hold promise as therapeutic agents for metastatic cancers.

EXPERIMENTAL PROCEDURES

Bacterial Expression and Purification of Wild-Type and Δ13C S100A4. Full-length human S100A4 was cloned into the NdeI/BamHI sites of the pET23a protein expression vector (Novagen Inc.), and the recombinant protein was purified as described previously (*29*). Protein yields of full-length S100A4 were typically 20 mg of purified protein per liter of bacterial culture. The Δ13C S100A4, in which the 13 C-terminal residues were deleted, was cloned into the NdeI/HindIII sites of the pET23a vector. For NMR, the S100A4 protein preparation was modified such that defined medium was used with ^{15}N-labeled NH_4Cl and $^{13}C_6$-labeled glucose as the only nitrogen and carbon sources, respectively, as described previously (*23*). Mass spectrometric analysis confirmed the purity of these proteins and indicated that the N-terminal methionine is not present in the purified protein (data not shown).

Peptides. The S100A4 C-terminal tail peptide (Ac-EFFEGFPDKQPRKK, corresponding to residues Glu88−Lys101 of S100A4), which comprises the immediate C-terminus of S100A4, was synthesized by Biosynthesis Inc. (Lewisville, TX). Myosin-IIA peptides (MIIA$^{1908-1923}$, Ac-DAMNREVSSLKNKLRR-$CONH_2$; FITC-MIIA$^{1908-1923}$, FITC-Ahx-DAMNREVSSLKNKLRR-OH; MIIA$^{1899-1923}$, Ac-ELEDATETADAMNREVSSLKNKLRR-$CONH_2$; MIIA$^{1893-1923}$, Ac-RRKLQRELEDATETADAMNREVSSLKNKLRR-$CONH_2$) were synthesized by Biosynthesis Inc. The FITC peptide used as a probe is not amidated on the C-terminus and has an aminohexanoic acid (Ahx) linker prior to the start of the peptide sequence. The molecular weight and purity (>95%) of all peptides were verified using mass spectrometry and HPLC, respectively. The concentration values for all peptide solutions were determined by quantitative amino acid analysis.

For experiments with FITC-MIIA$^{1908-1923}$, a 5 mM stock solution was prepared in 20 mM Tris (pH 7.5), 150 mM KCl, 1 mM DTT, and 0.02% NaN_3, aliquoted, and stored at −80 °C. A C-terminal fragment of the human myosin-IIA heavy chain that corresponds to residues 1851−1960 (MIIA$^{1851-1960}$) was cloned into the EcoRI/NdeI sites of pET23a. The myosin-IIA tail fragment (MIIA$^{1851-1960}$) was expressed in BL21-CodonPlus competent cells without induction (Stratagene, Cedar Creek, TX). Cell pellets were collected, resuspended in a lysis buffer containing 50 mM Tris (pH 7.5), 10% glycerol, 300 mM KCl, 2 mM DTT, 1 mM EDTA, 1 mM PMSF, and chymostatin, leupeptin, and pepstatin (5 μg/mL each), and frozen at −80 °C. Thawed cell pellets were sonicated, heated to 95 °C for 25 min, cooled on ice, and spun at 27000*g* for 20 min. The resulting supernatant was dialyzed against 20 mM Tris (pH 7.5) and 0.02% NaN_3 for subsequent purification on a High Q Sepharose anion exchange column. Fractions containing the myosin-IIA tail fragment were pooled and run on a Bio-Rad Bio-Scale Ceramic Hydroxyapatite type I column using a 0.005 to 0.4 M K_2HPO_4 gradient. The MIIA$^{1851-1960}$ protein concentration was determined using the modified Lowry assay (Pierce) and a MIIA$^{1851-1960}$ standard at a known concentration. The concentration of the MIIA$^{1851-1960}$ standard was determined by amino acid analysis (Keck Biotechnology Resource Laboratory at Yale University, New Haven, CT).

Protein Crystallization. The protein was dialyzed into 20 mM Tris (pH 7.5), 20 mM KCl, 10 mM DTT, 20 mM $CaCl_2$, and 0.02% NaN_3 and concentrated to 20−30 mg/mL (~0.85−1.28 mM dimer) using a 3000 MWCO Millipore Amicon centrifugal concentrator. Prior to crystallization, prochlorperazine (PCP) was added to a final concentration of 5 mM. Diffraction quality crystals were obtained by hanging drop vapor diffusion at 21 °C by mixing 1 μL of S100A4 and PCP with 1 μL of reservoir solution containing 0.05 M ammonium sulfate, 0.05 M Bis-Tris (pH 6.5), and 27.5% pentaerythritol ethoxylate (15/4 EO/OH) and equilibrating the samples against reservoir solution for 2−3 weeks. Diffraction from these crystals is consistent with space group $P3_221$ with two S100A4 chains per asymmetric unit and the following unit cell dimensions: $a = b = 52.4$ Å, $c = 140.4$ Å.

Structure Solution. Crystals of S100A4 with dimensions of 0.1 mm × 0.1 mm × 0.2 mm were flash-cooled in liquid nitrogen. Single anomalous dispersion (SAD) data (see Table 1) were collected at the X6A beamline (National Synchrotron

[1] Abbreviations: MIIA, nonmuscle myosin-IIA; LAR, leukocyte common antigen related; ITC, isothermal titration calorimetry; DTT, dithiothreitol; TSP, 3-(trimethylsilyl)propionic acid-d_4, sodium salt; HSQC, heteronuclear single-quantum coherence; NOESY, nuclear Overhauser effect spectroscopy; HOHAHA, homonuclear Hartmann−Hahn spectroscopy; HMQC, heteronuclear multiple-quantum coherence; DIPSI-2, decoupling in the presence of scalar interaction version 2; HPLC, high-performance liquid chromatography; TCEP, tris(2-carboxyethyl)phosphine; FITC, fluorescein isothiocyanate; BAPTA, 1,2-bis(*o*-aminophenoxy)ethane-*N*,*N*,*N*′,*N*′-tetraacetic acid; PCP, prochlorperazine; ACD, assembly competence domain.

Table 1: Dissociation Constants for Ca^{2+} Binding to S100A4

	[EF1] (μM)	[EF2] (μM)
S100A4 (low salt)	54.4 ± 10.8[a]	3.3 ± 1.3[a]
S100A4 (high salt)	>500[b]	2.6 ± 1.3[b]
S100A4 and $MIIA^{1851-1960}$ (high salt)	3.6 ± 0.2[c]	0.26 ± 0.01[c]

[a] The dissociation constants for Ca^{2+} binding to each S100A4 EF-hand domain were determined by ITC under low-salt conditions [20 mM Tris (pH 7.5), 20 mM KCl, and 250 μM TCEP]. [b] These values are from published studies (*71*). The dissociation constants for Ca^{2+} binding to each S100A4 EF-hand domain were determined using a 5,5′Br_2-BAPTA competition assay under high-salt conditions [20 mM Tris (pH 7.5), 150 mM KCl, 1 mM DTT, and 0.02% NaN_3]. [c] The dissociation constants for Ca^{2+} binding to each S100A4 EF-hand domain in the presence of $MIIA^{1851-1960}$ were determined using a 5,5′Br_2-BAPTA competition assay under high-salt conditions [20 mM Tris (pH 7.5), 150 mM KCl, 1 mM DTT, and 0.02% NaN_3].

Light Source, Brookhaven, NY) using an ADSC Q210 CCD detector (Area Detector Systems Corp., Poway, CA) and 1.7 Å wavelength radiation to enhance the anomalous signal from sulfur atoms and Ca^{2+} ions. Native data were collected on a Quantum 315 CCD detector (Area Detector Systems Corp.) with 1.0 Å wavelength radiation on the X29A beamline (National Synchrotron Light Source). Intensities were integrated using HKL2000 and reduced to amplitudes using TRUNCATE (*37, 38*). Experimental SAD phases were determined using SHELXD (*39*) and SHELXE (*40*), and the initial model was generated by the autobuilding algorithm in Arp/wArp (*41*). Further model building and refinement were performed with REFMAC and COOT (*38, 42*). The quality of the final structure was verified with composite omit maps, and the stereochemistry was checked with WHATCHECK (*43*) and PROCHECK (*44*). The final model contained two subunit chains of 96 residues each (Ala2−Gln97), four Ca^{2+} ions, and 226 water molecules with R_{cryst} and R_{free} values of 0.197 and 0.222, respectively. PCP was not visible in either the initial experimental or final refined electron density maps, even though diffraction quality crystals appeared only in the presence of the inhibitor. The LSQKAB and SSM algorithms were used for structural superimpositions (*38, 45*). Structural similarity with other S100 family members was analyzed using DALI (*46, 47*). Interhelix angles and distances were calculated using INTERHLX (*48*). Quaternary structure and accessible surface areas were analyzed using the PISA server using a 4 Å cutoff (http://www.ebi.ac.uk/msd-srv/prot_int/cgi-bin/piserver). Molecular contacts were analyzed with the program CONTACT (*38*).

NMR Spectroscopy. Purified S100A4 was dialyzed against Chelex-100-treated buffer, which included 0.1 mM Tris-d_{11} (pH 7.5) and 0.1 mM DTT, and then lyophilized, redissolved in a small aliquot of ddH_2O, and stored at −80 °C. The Ca^{2+}-loaded NMR samples contained an S100A4 subunit concentration of 0.25−1 mM, 0.34 mM NaN_3, 8 mM NaCl, 16 mM Tris-d_{11}, 0.1 mM EDTA, 6 mM DTT, 6 mM $CaCl_2$, and 10% D_2O. For all NMR samples, the pH was adjusted with cold HCl to 6.0 with continuous stirring. Prior to use, stock solutions of all buffer components were passed through a Chelex-100 column to remove any trace metals. NMR data were collected at 37 °C with either a Bruker DMX 600 NMR spectrometer (600.13 MHz for protons) or a Bruker Avance 800 US2 spectrometer (800.27 MHz for protons) both equipped with pulsed-field gradients, four frequency channels, and triple-resonance, *z*-axis gradient cryogenic probes. Unless otherwise stated, a 1 s relaxation delay was used and quadrature detection in the indirect dimensions was obtained with States−TPPI phase cycling (*49*). Data were processed on Linux workstations (Red Hat version 9.0) using the processing program NMRPipe (*50*). Time domain data in the indirect dimensions were extended by no more than one-third using standard linear prediction routines (*51*), except for data in constant time domains that were extended 2-fold using mirror-image linear prediction (*52*). All proton chemical shifts are reported with respect to the H_2O or HDO signal taken as 4.658 ppm relative to external TSP (0.0 ppm) at 37 °C. The ^{13}C and ^{15}N chemical shifts were indirectly referenced using the following ratios of zero-point frequencies at 37 °C: 0.10132905 for ^{15}N to ^{1}H and 0.25144953 for ^{13}C to ^{1}H (*53–55*).

Uniformly ^{15}N-labeled S100A4 was used to collect the two-dimensional (2D) $^{1}H-^{15}N$ fast HSQC spectrum (*56*), the three-dimensional (3D) ^{15}N-edited NOESY-HSQC spectrum with a 100 ms mixing time (*57*), the 3D ^{15}N-edited HOHAHA-HSQC spectrum with a 60 ms DIPSI-2rc spin-lock and a 10 kHz rf field strength (*58, 59*), and the 3D ^{15}N-edited HMQC-NOESY-HSQC spectrum with a 125 ms mixing time (*60*). A uniformly ^{13}C- and ^{15}N-labeled S100A4 sample was used to conduct the 3D CBCA(CO)NH (*61, 62*), 3D HNCACB (*63*), 3D HN(CO)CA (*64*), and HNCA (*65*) triple-resonance NMR experiments. In all of the ^{15}N-edited experiments, the fast-HSQC detection scheme was incorporated into the sequence to avoid water saturation, and undesired magnetization was alleviated using pulsed field gradients throughout the various NMR pulse sequences (*66*).

Thermodynamic Binding Studies. Binding of Ca^{2+} and myosin-IIA peptides to apo-S100A4 and Ca^{2+}-S100A4, respectively, was analyzed by measuring heat changes using a VP-ITC titration microcalorimeter (MicroCal, Inc., Northampton, MA). All protein, peptide, and metal solutions were degassed under vacuum and equilibrated at 37 °C prior to titration. The sample cell (1.4 mL) contained 20 mM Tris (pH 7.5), 20 mM KCl, 250 μM TCEP, and 75 μM S100A4 in the Ca^{2+} titrations with *c* values ranging between 5 and 200. The S100A4-containing buffer described above was supplemented with 800 μM $CaCl_2$ for titrations monitoring myosin-IIA peptide binding to Ca^{2+}-S100A4. In all titrations, the reference cell contained water. Stock concentrations for injection of the titrant were 3 mM $CaCl_2$ and 0.5 mM $MIIA^{1893-1923}$, with all of the other buffer conditions matched to the sample. Solutions were injected in 5 μL aliquots using the default injection rate of 10 s with a 360 s interval between injections, which allowed the trace to return to baseline before the next injection. The resulting titration curves were corrected for the protein-free buffer control and analyzed using the Origin for ITC software supplied by MicroCal.

Fluorescence anisotropy measurements were performed at 22 °C using a Fluoromax-3 spectrofluorometer (Jobin Yvon Inc.). Individual reaction mixtures (200 μL) contained 100 nM FITC-$MIIA^{1908-1923}$ and 0−30 μM S100A4 dimer in 20 mM Tris (pH 7.5), 150 or 20 mM KCl, 1 mM DTT, 0.02% NaN_3, and 0.5 mM $CaCl_2$. Anisotropy was measured with excitation at 494 nm and emission at 516 nm. Measurements were acquired at the magic angle corresponding to the angle of 55° between the vectors of polarization of the excitation and emission light using a *G* factor of 0.634 previously determined for FITC on this instrument. Competition assays with $MIIA^{1893-1923}$ and $MIIA^{1851-1960}$ contained 15 μM

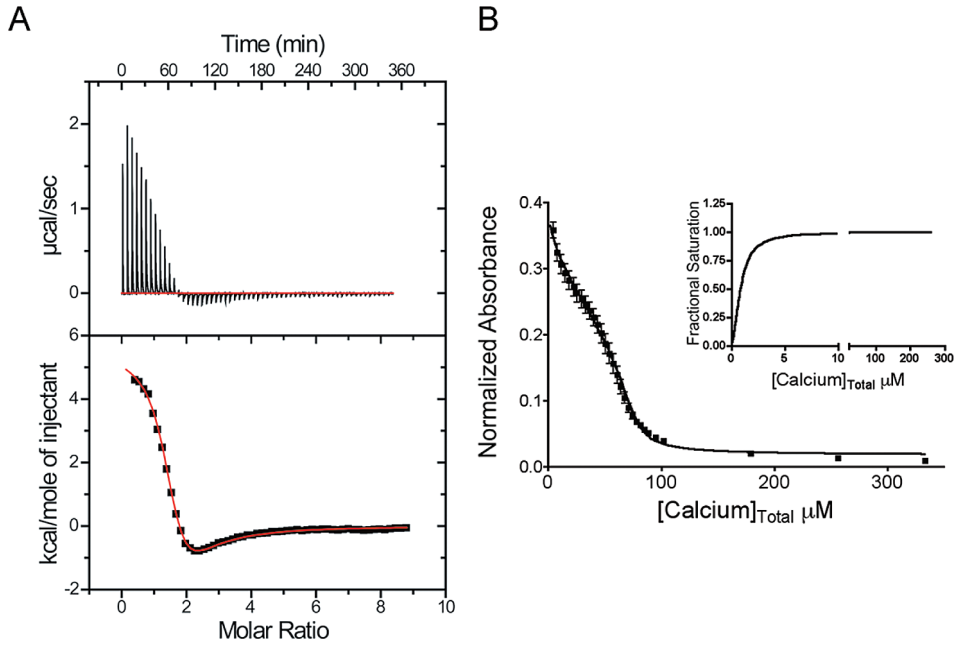

FIGURE 1: Thermodynamic data showing Ca^{2+} binding to S100A4. (A) Isothermal titration calorimetry (ITC) data demonstrating the interaction of S100A4 with Ca^{2+} ($n = 2$). (B) Competition assay with the chelator 5,5′Br_2-BAPTA to examine the affinity of S100A4 for Ca^{2+} in the presence of $MIIA^{1851-1960}$. The decrease in absorbance was monitored at 263 nm for a mixture containing 25 μM 5,5′Br_2-BAPTA, 12.5 μM S100A4 dimer, and 125 μM $MIIA^{1851-1960}$. The inset shows the saturation curve representation for the best fit in Caligator.

S100A4 dimer, 100 nM FITC-$MIIA^{1908-1923}$, 0.3 mM $CaCl_2$, and 0−40 and 0−30 μM peptide, respectively, in 20 mM Tris (pH 7.5), 150 or 20 mM KCl, 1 mM DTT, 0.02% NaN_3, and 0.5 mM $CaCl_2$. Controls included experiments representing maximum anisotropy (15 μM S100A4, 100 nM FITC-$MIIA^{1908-1923}$, and calcium) and minimum anisotropy (100 nM FITC-$MIIA^{1908-1923}$ and calcium). Experiments were performed in triplicate and results fit to a sigmoidal dose−response equation with a variable slope to obtain the EC_{50} value. Using this value, the dissociation constant for the peptides was obtained using the equation $K_d = (K_{dP}EC_{50})/[S]$, where EC_{50} is the concentration at half-maximal binding of the competing peptide determined from fitting the raw data, K_{dP} is the dissociation constant for binding of FITC-$MIIA^{1908-1923}$ to S100A4, and [S] represents the concentration of S100A4 dimer.

Ca^{2+} binding affinities for EF1 and EF2 of S100A4 in the presence of myosin-IIA were determined using a 5,5′Br_2-BAPTA competition assay as described previously (*67*). Calcium was titrated into a solution containing 25 μM 5,5′Br_2-BAPTA, 12.5 μM S100A4 dimer, and 125 μM $MIIA^{1851-1960}$ at 25 °C in 20 mM Tris (pH 7.5), 150 mM KCl, 1 mM DTT, and 0.02% NaN_3, and the decrease in absorbance was monitored at 263 nm. The total amount of Ca^{2+} in the protein preparation was less than 0.1 mol of Ca^{2+}/mol of protein. Using Caligator, averaged data from five titrations from four independent experiments were fit to two Ca^{2+} binding sites using a stepwise macroscopic binding equation in the presence of chelator (*68*).

Analytical Ultracentrifugation. Sedimentation equilibrium and velocity experiments were performed with a Beckman XL-I analytical ultracentrifuge equipped with absorbance optics and a Ti60 rotor at 25 °C. The sedimentation boundaries were monitored at 280 nm. Wild-type and Δ13C S100A4 were dialyzed into a buffer containing 20 mM Tris (pH 7.5), 150 mM KCl, 1 mM TCEP, 0.02% NaN_3, and either 10 mM $CaCl_2$ (Ca^{2+}-bound) or 2 mM EDTA and 2 mM EGTA (Ca^{2+}-free). Sedimentation velocity experiments were conducted at 55000 rpm using double-sector centerpieces. S100A4 subunit concentrations from 10 to 100 μM were analyzed [DCDT+ version 2.0.9 (*69*)]. Sedimentation equilibrium experiments were conducted using six-channel centerpieces; three concentrations of protein were analyzed for each experiment (wild-type Ca^{2+}-bound S100A4, 28, 54, and 74 μM; wild-type apo-S100A4, 23, 38, and 52 μM; Ca^{2+}-bound Δ13C S100A4, 39, 61, and 90 μM). The absorbance scans obtained following 24 h equilibrations at 15000 and 22000 rpm were globally analyzed using HeteroAnalysis version 1.0.114 (J. L. Cole and J. W. Lary, Analytical Ultracentrifugation Facility, Biotechnology Services Center, University of Connecticut, Storrs, CT) for the weight-average molecular weight or the dimer−tetramer equilibrium constant. The ν-bar values of 0.7346 and 0.7337 were calculated from the amino acid composition of wild-type S100A4 and Δ13C S100A4, respectively. Density and viscosity values were provided by Sednterp version 1.06 (B. Hayes, T. Laue, and J. Philo, Sedimentation Interpretation Program, 2003, University of New Hampshire, Durham, NH). The best-fit parameters and their 95% joint confidence intervals are reported. The calculated masses of wild-type S100A4 and Δ13C S100A4 monomers are 11597 and 9991.4 Da, respectively.

RESULTS

Ca^{2+} binding to Apo-S100A4. Like all S100 proteins, S100A4 has a pseudo-EF-hand (residues Ser20−Glu33; EF1) and a typical EF-hand (residues Asp63−Glu74; EF2). Since the interaction between S100A4 and target proteins such as MIIA depends on Ca^{2+} binding to the typical EF-hand, we examined the Ca^{2+} binding properties of S100A4 (*70, 71*). Under low-salt conditions used for NMR, human S100A4 binds two Ca^{2+} ions with the high-affinity site (EF2; $^{Ca2}K_d = 3.3 \pm 1.3$ μM) exhibiting a dissociation constant that is 1 order of magnitude tighter than that of the low-affinity site [EF1; $^{Ca1}K_d = 54 \pm 11$ μM (Figure 1 and Table 1)]. As

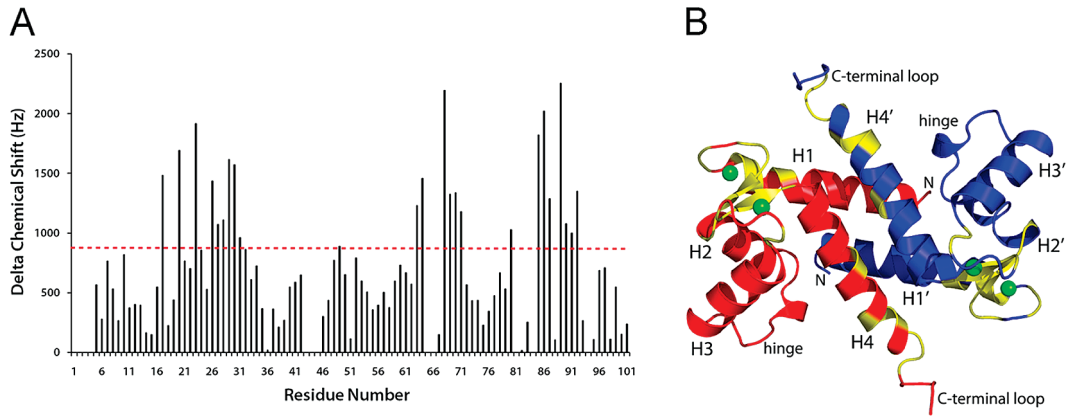

FIGURE 2: Chemical shift perturbations following the addition of Ca^{2+} to apo-S100A4. (A) Bar graph of the cumulative ^{1}H, ^{15}N, and ^{13}C chemical shift perturbations observed per residue upon the addition of Ca^{2+} to apo-S100A4. (B) Ribbon diagram of Ca^{2+}-S100A4 showing the subunits in red and blue. Residues highlighted in yellow exhibited the largest perturbations (as per the dashed red line at 900 Hz in panel A).

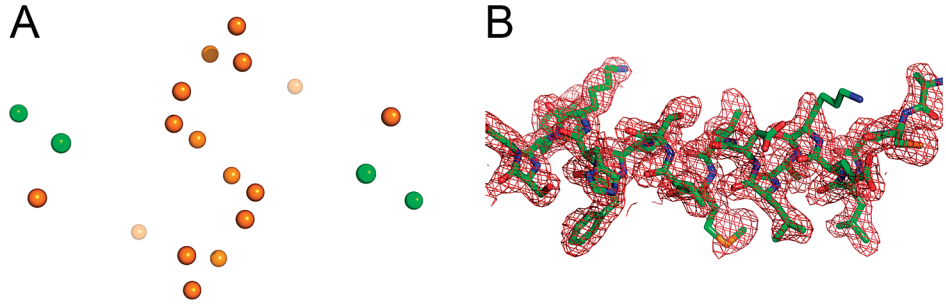

FIGURE 3: (A) Heavy atom positions detected by SHELXD based on the SAD signal at 1.7 Å wavelength. Green and orange spheres denote Ca^{2+} ions and sulfur atoms, respectively. (B) Refined model of S100A4 (residues Ala2−Gly21) superimposed onto the $2F_o - F_c$ electron density map, contoured at 1σ.

reported previously, at physiological salt levels the high-affinity site on S100A4 binds Ca^{2+} with a similar K_d ($^{Ca2}K_d = 2.6 \pm 1.0$ μM), but the pseudo-EF-hand shows no appreciable affinity for Ca^{2+} (*70–73*). At physiological salt levels in the presence of a myosin-IIA peptide ($MIIA^{1851-1960}$), the Ca^{2+} binding affinity of S100A4 in both the pseudo-EF- and typical EF-hands increases by more than 1 order of magnitude [$^{Ca1}K_d = 3.6 \pm 0.2$ μM; $^{Ca2}K_d = 0.26 \pm 0.01$ μM (Figure 1 and Table 1)].

To determine which amino acid residues in human S100A4 were most affected by Ca^{2+} binding in solution, Ca^{2+} titrations of human apo-S100A4 were monitored using NMR spectroscopic methods. Upon addition of Ca^{2+}, most S100A4 resonances disappeared and then reappeared with new chemical shift values consistent with Ca^{2+} binding to S100A4 in the slow exchange regime on the NMR chemical shift time scale. In such a binding regime, the shifted correlations of Ca^{2+}-S100A4 could not be followed during the titration and required that they be completely reassigned a priori. The largest of these chemical shift perturbations (>900 Hz) are clustered in the two EF-hand Ca^{2+}-binding loops and in helix 4 (Figure 2), which is consistent with Ca^{2+} binding to both EF-hands. In addition to these largest perturbations, significant changes in chemical shift (>200 Hz) were observed for numerous other residues throughout the protein and support the notion that a significant conformational change occurs in human S100A4 upon binding Ca^{2+}, as reported previously for murine S100A4 (*74*).

Structure Determination. Initial attempts to determine the S100A4 structure using molecular replacement methods with several existing NMR structures of S100 family members, including rat S100B (PDB entry 1DT7), rabbit S100A6 (PDB entry 1JWD) and human apo-S100A4 (PDB entry 1M31), were not successful. The excellent diffraction quality and relatively high symmetry of the S100A4 crystals suggested that sulfur SAD might be feasible. The four methionine residues, four cysteine residues, and two Ca^{2+} ions present in this 101-amino acid protein were expected to yield a significant anomalous signal when data were collected with 1.7 Å radiation. Indeed, all four Ca^{2+} ions and most of the sulfur atoms in the asymmetric unit (containing two protein chains) were located with SHELXD (Figure 3A), allowing near-automated tracing of the entire structure (Figure 3B). In the final refined model, 92.0, 6.9, and 1.1% of residues fall into the favorable, allowed, and generous areas of the Ramachandran plot, respectively (Table 2) (*44*). Residues with less favorable backbone conformations are located in the conformationally flexible loops of S100A4.

Three-Dimensional Structure of Ca^{2+}-S100A4. Most of the crystallized S100A4 construct is well-defined in the experimental electron density map except for residues at the extreme C-terminus, Pro98−Lys101, which are not included in the model. Typical of the S100 family, each of the two S100A4 chains in the asymmetric unit is predominantly α-helical with four major helices per chain denoted H1−H4 (Figure 4A). As with other S100 protein family members, helices 1 and 4 from one subunit are arranged in an antiparallel manner with helices 1′ and 4′ of the second subunit to form an X-type four-helix bundle at the dimer interface. The two independent chains superimpose with a rms deviation of 0.71 Å for all Cα atoms with the most

Table 2: Crystallographic Data and Refinement Statistics

	SAD	native
Data collection		
beamline	NSLS-X6A	NSLS-X29A
wavelength (Å)	1.7	1.0
resolution limits (Å)	20−1.95	20−1.63
no. of observed reflections	299244	288354
no. of unique reflections	16952	28584
completeness (%)	89.4 (50.2)[a]	99.9 (99.9)[a]
R_{merge}[b]	0.053 (0.367)[a]	0.096 (0.685)[a]
Refinement Statistics		
no. of protein non-hydrogen atoms	2458	
no. of water molecules	226	
R_{cryst}[c]	0.197 (0.245)[a]	
R_{free}[c]	0.222 (0.302)[a]	
average *B*-factor (Å^2)	25.1	
rmsd from Ideality		
bond lengths (Å)	0.013	
bond angles (deg)	1.4	
torsion angles (deg)	23.1	
Ramachandran plot		
core	92.0%	
allowed	6.9%	
generous	1.1%	

[a] Values in parentheses indicate statistics for the high-resolution bin. [b] $R_{merge} = \sum_j|I_j(hkl) - \langle I(hkl)\rangle|/\sum\sum_j|\langle I(hkl)\rangle|$, where I_j is the intensity measurement for reflection j and $\langle I\rangle$ is the mean intensity over j reflections. [c] $R_{cryst}/R_{free} = \sum||F_o(hkl)| - |F_c(hkl)||/\sum|F_o(hkl)|$, where F_o and F_c are observed and calculated structure factors, respectively. No σ cutoff was applied. Five percent of the reflections were excluded from refinement and used to calculate R_{free}.

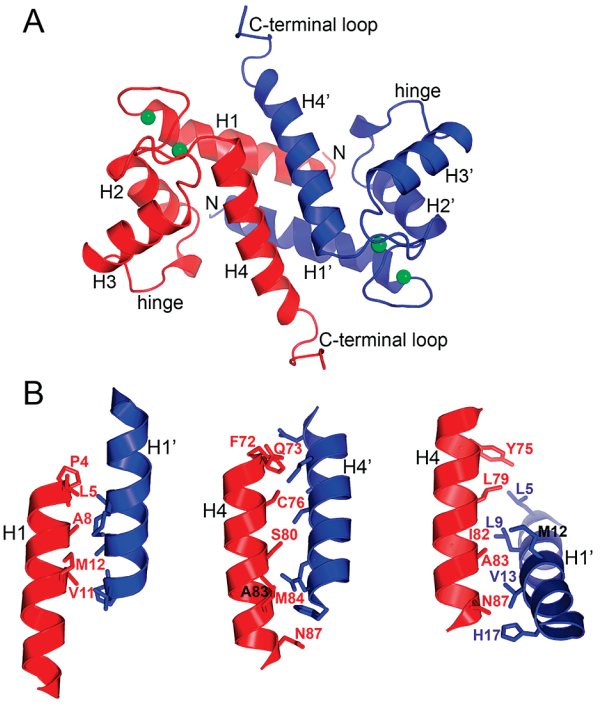

FIGURE 4: Molecular architecture of the Ca^{2+}-S100A4 dimer. (A) Ribbon diagram of the dimer, where the two subunits are colored blue and red. The key structural elements common for the S100 family are indicated. Green spheres denote Ca^{2+} ions. (B) Details of the dimer interface of S100A4 involving helix 1−1′, 4−4′, and 1−4′ (1′−4) contact areas.

significant differences of ~1.9 Å residing in the conformationally flexible C-terminal tail (residues Phe89−Gln97).

Several Ca^{2+}-S100 structures have been determined by X-ray crystallography and NMR (Table 3). A DALI search

Table 3: Structural Differences between Apo and Ca^{2+}-S100A4 and Other S100 Proteins

	rms deviation between C_α atoms (Å)/*Z* score[a]		sequence identity (%)
	apo[b]	Ca^{2+}-bound[c]	
S100A1	3.2/7.3[d] (86)	2.6/10.3[e] (92)	49
S100A6	2.1/9.6[f] (84)	1.5/15.1[g] (89)	50
S100A7	n/a	2.3/11.3[h] (87)	27
S100A8	n/a	2.2/13.3[i] (88)	34
S100A9	n/a	1.3/13.0[j] (81)	32
S100A11	3.2/7.0[k] (87)	2.0/14.5[l] (95)	27
S100A12	n/a	1.5/14.3[m] (87)	40
S100A13	3.7/7.0[n] (83)	1.5/14.5[o] (86)	34
S100B	3.5/8.4[p] (88)	2.4/11.7[q] (92)	48
calbindin D9K	3.1/4.6[r] (67)	1.9/11.7[s] (73)	38
calcyclin	2.9/9.1[t] (87)	2.8/10.5[u] (88)	51

[a] Calculated using DaliLite (*47*); values in parentheses indicate the number of superimposed atoms. [b] PDB entry 1M31 (*23*). [c] PDB entry 2Q91 (this work). [d] PDB entry 1K2H (*77*). [e] PDB entry 1ZFS (*35*). [f] PDB entry 1K9P (*76*). [g] PDB entry 1K96 (*76*). [h] PDB entry 1PSR (*100*). [i] PDB entry 1MR8 (*105*). [j] PDB entry 1IRJ (*106*). [k] PDB entry 1NSH (*95*). [l] PDB entry 1QLS (*96*). [m] PDB entry 1E8A (*107*). [n] PDB entry 1YUR (*97*). [o] PDB entry 2H2K (*98*). [p] PDB entry 1SYM (*78*). [q] PDB entry 1QLK (*34*). [r] PDB entry 1KCY (*108*). [s] PDB entry 4ICB (*108*). [t] PDB entry 2CNP (*75*). [u] PDB entry 1JWD (*99*).

for homologous structures reveals that the most structurally similar dimeric S100 family member is human S100A6 with a *Z* score of 15.1 and a rms deviation of 1.5 Å. The most significant structural differences between S100A4 and S100A6 occur in the hinge region between helices 2 and 3 (residues Leu42−Asp51). Interestingly, monomeric Ca^{2+}-calbindin is also very similar to S100A4 with a *Z* score of 11.7 and a rms deviation of 1.9 Å (Table 3). The positions and orientations of helices 1−4 in the two proteins are comparable (Table 4) with the largest conformational difference of ~12 Å occurring in the hinge region. Notably, in calbindin, the relative orientations of helices 1 and 4 (crucial elements of the dimer interface in S100 proteins) are well preserved, even though the helices are significantly shorter than in S100A4.

The two S100A4 chains in the asymmetric unit interact to form a tight dimer with an interface that is observed throughout the S100 family. The dimer interface buries 3225 Å^2 of accessible surface area, 86% of which is contributed by helix 1 (residues Pro4−Ser20) and helix 4 (residues Phe72−Glu88) (Figure 4 and Table 5). There are a total of 34 residue-to-residue interchain contacts. Of these, 10 contacts are between helices 1 and 1′, 12 contacts between helices 4 and 4′, and 12 contacts between helices 1 and 4′ and helices 1′ and 4 (Figure 4B). There are 12 hydrogen bonds within the dimer interface, some of which are asymmetric (Glu6 $O_{\epsilon1}$−Ser44′ O_γ, Glu6 $O_{\epsilon2}$−Ser44′ O_γ, Glu6 $O_{\epsilon2}$−Ser43′ N, His17 $N_{\epsilon2}$−Asn87′ $O_{\delta1}$, and their symmetry mates). In addition, hydrogen bonds are observed between Ser80 O_γ and Ser80′ O_γ, Ser80 O_γ and Ser44′ N, Lys26 N_ζ and Glu91′ $O_{\epsilon1}$, and Lys26 N_ζ and Glu91′ $O_{\epsilon2}$. In homologous S100 structures, the predominantly nonpolar nature of the subunit interface is conserved, but the actual degree of sequence conservation is low. For example, among four S100 structures with at least 48% overall sequence identity to S100A4 (Table 3) (*75*–*78*), only five of 23 interface residues (21.7%) are conserved, indicating a higher than average level of sequence variability of the dimer interface in the S100 family.

Table 4: Interhelical Angles and Distances in S100A4[a]

	interhelical angle (deg)								interhelical distance (Å)	
	1−2	1−3	1−4	2−3	2−4	3−4	1−1′	4−4′	1−1′	4−4′
Ca^{2+}-S100A4	139 ± 1	−118 ± 2	130 ± 2	102 ± 2	−32 ± 2	107 ± 2	−151 ± 1	145 ± 1	13.9 ± 0.5	10.1 ± 0.5
apo-S100A4[b]	119 ± 2	−55 ± 4	120 ± 2	151 ± 4[f]	−45 ± 3	162 ± 4	−152 ± 4	153 ± 4	n/a	n/a
Ca^{2+}-S100A1[c]	132 ± 1	−102 ± 2	131 ± 2	125 ± 2	−29 ± 1	121 ± 2	−157 ± 3	152 ± 3	12.5 ± 0.2	11.1 ± 0.4
apo-S100A1[d]	120 ± 3	−45 ± 2	107 ± 2	148 ± 2	−46 ± 1	−150 ± 1	−165 ± 3	176 ± 2	n/a	n/a
calbindin[e]	129 ± 1	−116 ± 2	123 ± 2	111 ± 2	−31 ± 1	118 ± 2	n/a	n/a	n/a	n/a

[a] The helices in S100A4 are defined as follows: helix 1, Pro4−Ser20; helix 2, Lys31−Glu41; helix 3, Glu52−Leu62; helix 4, Phe72−Glu88. [b] From ref *23*. [c] From ref *35*. [d] From ref *77*. [e] From ref *108*. [f] In the orginal report (*23*), the interhelical angle for helices 2 and 3 in apo-S100A4 was mistakenly reported as a negative value.

Table 5: Residues at the Dimer Interface of S100A4

helix 1 − 1′ interactions										
position	4	5	8	11	12					
residue	P	L	A	V	M					
helix 4 − 4′ interactions										
position	72	73	76	80	83	84	87			
residue	F	Q	C	S	A	M	N			
helix 1 − 4′ interactions										
position	5	9	12	13	17	75	79	82	93	87
residue	L	L	M	V	H	Y	L	I	A	N

Ca^{2+} Coordination in S100A4. Calcium ions bind to the pseudo-EF- and typical EF-hands at sites located between helices 1 and 2 and helices 3 and 4, respectively. In the pseudo-EF-hand, the Ca^{2+} ion is coordinated by the main chain carbonyl oxygens of Ser20, Glu23, Asp25, and Lys28; the side chain carboxylate of Glu33 (both oxygen atoms); and a water molecule (Figure 5A). Thus, the pseudo-EF-hand primarily coordinates Ca^{2+} with main chain carbonyl oxygen atoms. In the C-terminal typical EF-hand, the Ca^{2+} ion is coordinated by the side chains of Asp63, Asn65, Asp67, and Glu74 (both oxygen atoms); the carbonyl oxygen of Glu69; and a water molecule (Figure 5B). In both EF-hands, the Ca^{2+} ion is coordinated by seven oxygen atoms with average ion−oxygen distances of 2.4 Å, which is similar to those of other crystallographically determined S100 structures (Table 3). NMR and X-ray structures of related family members (e.g., S100B) show similar Ca^{2+} coordination in the typical EF-hand with contributions from carboxylate oxygen atoms in the *X*, *Y*, *Z*, −*Z*, and −*Z*′ positions and from a backbone carbonyl oxygen in the −*Y* position. The

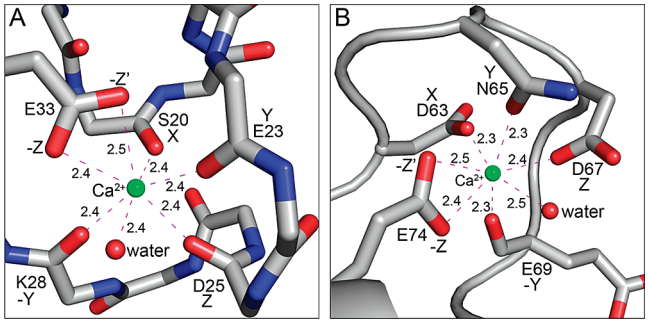

FIGURE 5: Structures of the Ca^{2+}-loaded S100A4 EF-hands. (A) N-Terminal pseudo-EF-hand. The Ca^{2+} ion is coordinated by the main chain carbonyl oxygens of Ser20, Glu23, Asp25, and Lys28; the side chain carboxylate of Glu33 (both oxygens), and a water molecule. (B) C-Terminal typical EF-hand. The Ca^{2+} ion is coordinated by the side chains of Asp63, Asn65, Asp67, and Glu74 (both oxygens); the carbonyl oxygen of Glu69; and a water molecule. Green and red spheres denote Ca^{2+} and water atoms, respectively.

final coordination position (−*X*) is occupied by a water molecule in the X-ray structure, which could not be observed experimentally by NMR. In contrast, the NMR structure of Ca^{2+}-S100B and the X-ray structure of Ca^{2+}-S100A4 exhibit differences in Ca^{2+} coordination at the pseudo-EF-hand. Specifically, the NMR-based model, which relied heavily on lanthanide luminescence data (*79*), identified only four protein ligands and required modeling together with the NMR data to predict the Ca^{2+} ligands, whereas in the X-ray structures of Ca^{2+}-S100B and Ca^{2+}-S100A4, all seven protein ligands to oxygen are observed (*34, 79*). This discrepancy in Ca^{2+} coordination can be attributed to the high mobility exhibited by several regions of S100B in solution, which has been observed on multiple time scales using ^{15}N relaxation NMR measurements for both S100B and S100A4 (*80*) (unpublished observations) and may account for why the pseudo-EF-hand binds Ca^{2+} more weakly than the typical EF-hand. In addition, despite identical coordination numbers and protein−ion distances, the reduced Ca^{2+} affinity exhibited by the pseudo-EF-hand may result from the required conformational adjustment of the four main chain carbonyl oxygen atoms within the pseudo-EF-hand (*81*). These adjustments may be more energetically costly than positioning the more flexible side chains within the typical EF-hand.

Ca^{2+} Switch in S100A4. It is well-appreciated that S100A4 undergoes a Ca^{2+}-dependent conformational rearrangement, which is required for the recognition and binding of its various protein targets (*8*). For the first time, this conformational change can be described at atomic resolution by comparing the structures of the apo and Ca^{2+}-loaded forms of S100A4. Specifically, the interhelical angle between helices 3 and 4 in each subunit of apo-S100A4 is 162 ± 2°, and in the Ca^{2+}-bound state, it is 107 ± 2°, indicating a Ca^{2+}-dependent change of −55°. Changes of −63° and −49° in the interhelical angles between helices 1 and 3 and helices 2 and 3, respectively, are observed as well (Figure 6A and Table 4). Accompanying these large helix movements are numerous reorientations of residues that are critical for coordination of Ca^{2+} (Figure 6B,C). Upon Ca^{2+} activation, helices 3 and 2 move most (55° and −23°, respectively) whereas helices 1 and 4 move least (1° and 12°, respectively) relative to their positions in the apo state. This is not surprising given that helices 1 and 4 are locked in the core of the dimer interface.

As a result of the reorientation of helix 3, the number of residue contacts between helices 3 and 4 decreases from four to three and the number of contacts between helices 3 and 2 increases from six to eight, including the formation of two new hydrogen bonds, Lys35−Glu52 and Lys31−Gln56. In addition, residues that line the peptide binding pocket in

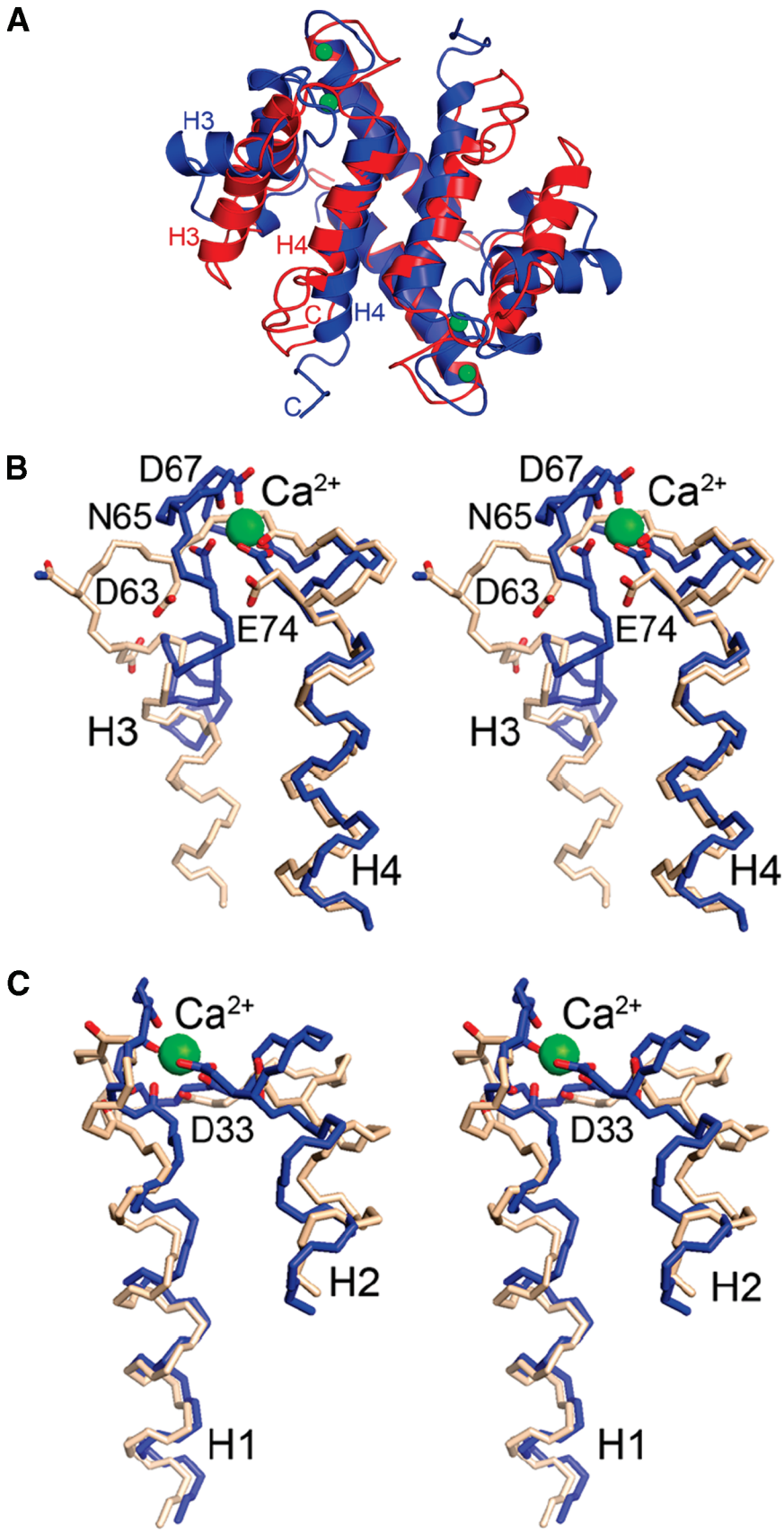

FIGURE 6: Conformational rearrangements in S100A4 caused by Ca^{2+} binding. (A) Ribbon diagrams comparing the three-dimensional structures of apo-S100A4 (red) and Ca^{2+}-S100A4 (blue). Green spheres denote Ca^{2+} ions. Stereoviews of the (B) pseudo-EF-hand and (C) typical EF-hand of apo-S100A4 (beige) and Ca^{2+}-S100A4 (blue). The Ca^{2+}-coordinating oxygen atoms are colored red in both the apo and Ca^{2+}-bound states.

Ca^{2+}-S100A4 are subject to dramatic shifts to achieve their productive binding conformation. For example, the side chain of Phe45 moves ~14 Å from a solvent-exposed environment in apo-S100A4 to a location at the bottom of the binding

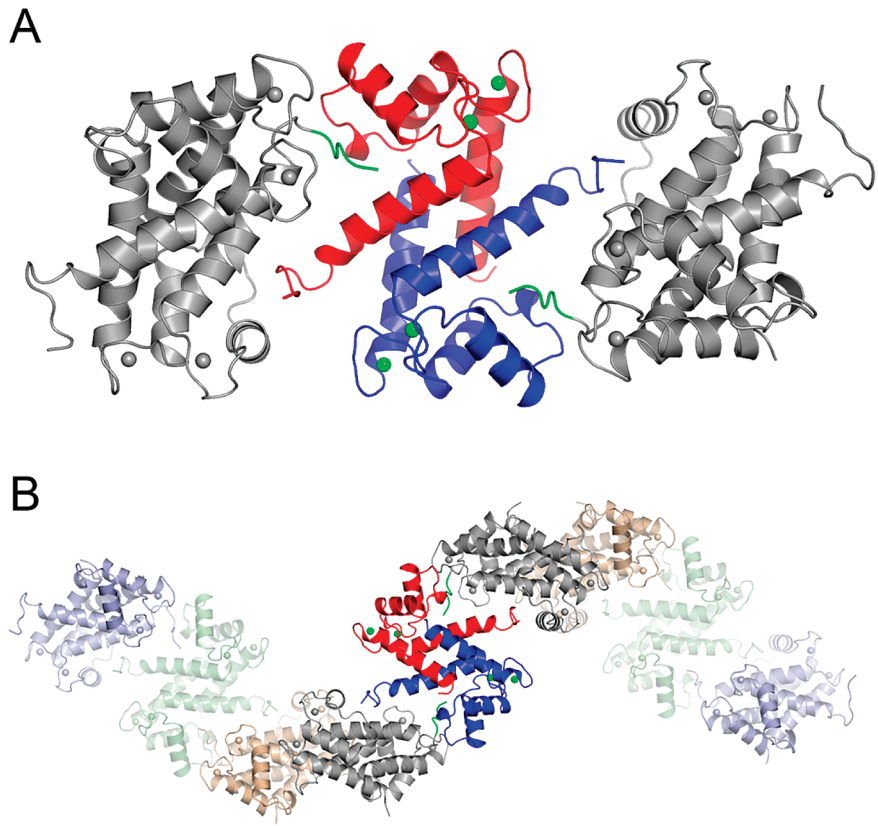

FIGURE 7: Self-association of S100A4 molecules in the crystal lattice. (A) The S100A4 dimer is shown with one red and one blue subunit. The symmetry-related molecules (gray) in the S100A4 crystals are positioned such that their C-terminal tails (green) bind to the hydrophobic cleft of the central molecule. (B) The interacting S100A4 dimers form infinite superhelical structures in the crystal.

pocket where it interacts with the side chain of Phe78 from helix 4. Leu46 which is buried in a hydrophobic cluster with residues Leu38, Leu42, Ile82, and Met85 in apo-S100A4 positions next to Leu38, Phe45, Ala54, Phe55, and Leu58. In the Ca^{2+}-S100A4 dimer, the guanidinium group of Arg49 moves from a solvent-exposed position to the edge of the binding pocket to form a salt bridge with the carboxylate of Asp51. Lys57 moves away from Pro91 in apo-S100A4 to the edge of the pocket and forms a hydrogen bond with Asn61. In the Ca^{2+}-S100A4 dimer, Asn61, Phe78, Cys81, and Met85 shift slightly to adjust to the new positions of the above-mentioned residues. These substantial side chain movements are consistent with the large chemical shift perturbations that are detected upon addition of Ca^{2+} in our NMR studies (Figure 2).

Crystal Packing Interactions. An examination of the crystal packing interactions shows that the C-terminal tail (residues Glu91−Gln97) of each S100A4 chain interacts with the deep cleft formed between helices 3 and 4 of the 2-fold crystallographically related molecule (Figure 7A). This pocket in other S100 proteins generally functions as the target recognition cleft. As a result of these interactions, a left-handed superhelix of S100A4 dimers is observed that runs parallel to the crystallographic *c*-axis (Figure 7B). Many of the interdimeric interactions between the C-terminal tail of one dimer and the target binding cleft of the symmetry related molecule are nonpolar, involving residues Glu91−Gln97 of the C-terminal tail and residues Phe45, Leu46, Arg49, Lys57, Asn61, Phe78, Cys81, and Met85 of the binding pocket (Figure 8). Of a total of 19 residue-to-residue contacts, only three are direct hydrogen bonds, and several more are indirect hydrogen bonds mediated by water molecules. The side

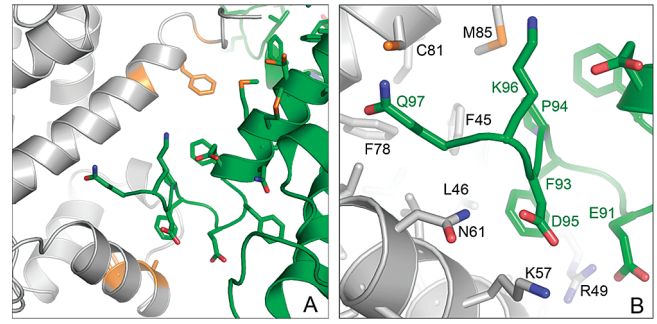

FIGURE 8: Interaction of the C-terminal tail of S100A4 (green) with the ligand binding site of the symmetry-related S100A4 molecule (gray). (A) Overall view of the ligand binding pocket. Residues showing chemical shift perturbations upon binding a peptide derived from the C-terminus of S100A4 (residues Glu88−Lys101) are colored orange. (B) Zoomed in view. Many of the interactions are nonpolar; however, Glu91 and Asp95 of the peptide may form ionic interactions with Arg49, Asn61, and Lys57 from the symmetry-related molecule.

chains of Glu91 and Asp95 exhibit weak density and relatively high *B*-factors, although they can be modeled to participate in potential ionic interactions with Arg49, Asn61, and Lys57, respectively, in the pocket. The most C-terminal residues (Pro98−Lys101) are not visible in the electron density map.

Binding of the S100A4 C-Terminal Tail to Ca^{2+}-S100A4. To determine whether the packing interactions observed by X-ray crystallography between the C-terminal tail and the peptide binding pocket also occur in solution, binding of a peptide derived from the C-terminus of S100A4 (residues Glu88−Lys101) was examined using NMR spectroscopy.

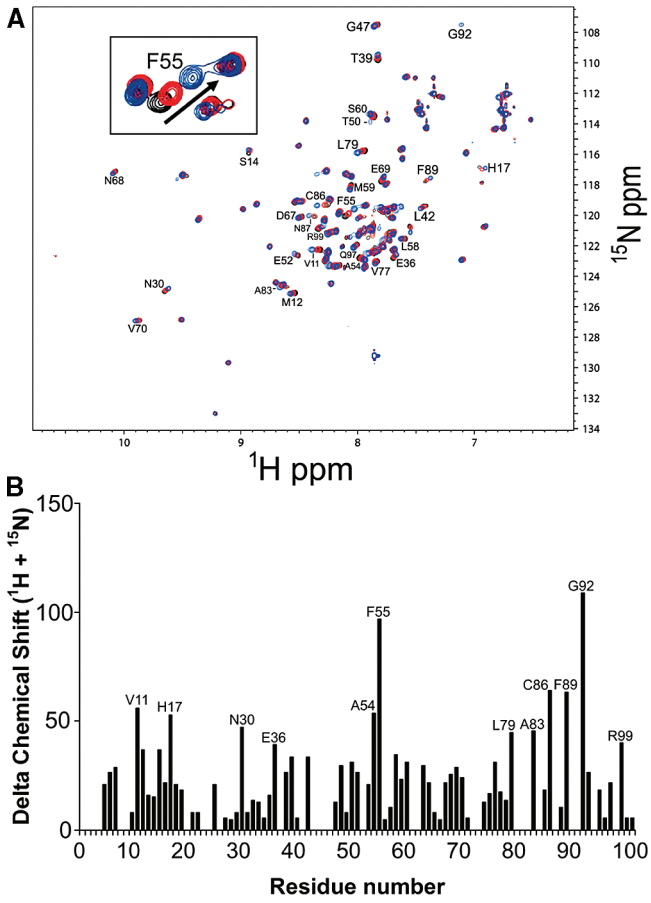

FIGURE 9: Chemical shift perturbations of $^{1}H-^{15}N$ correlations in a 2D HSQC spectrum of Ca^{2+}-S100A4 upon the addition of a peptide derived from the C-terminus of S100A4. (A) HSQC spectra of Ca^{2+}-S100A4 in the absence (black contours) and presence of 0.6 mM (red contours) and 3.6 mM (blue contours) C-terminal S100A4 peptide. The inset shows an expanded region of the HSQC spectrum illustrating the perturbations to the $^{1}H-^{15}N$ correlation for F55. (B) Chemical shift perturbations for residues in Ca^{2+}-S100A4 upon addition of 3.6 mM C-terminal S100A4 peptide.

In the absence of Ca^{2+}, there were no chemical shift perturbations upon the addition of peptide; however, in the presence of Ca^{2+}, perturbations in $^{1}H-^{15}N$ correlations were observed (>40 Hz) for residues Val11, His17, Asn30, Glu36, Ala54, Phe55, Leu79, Ala83, Cys86, Phe89, Gly92, and Arg99 (Figure 9), which is consistent with this peptide binding to the target binding cleft of S100A4. The assignment of these resonances in the presence of peptide was straightforward because peptide binding was in the fast exchange regime on the chemical shift time scale, which allowed the movements of the correlations to be followed easily. The perturbation of these specific residues is consistent with the interactions observed between dimer units of S100A4 in the X-ray crystal structure; however, peptide binding was weak with a K_d of 1.05 ± 0.10 mM.

Analytical sedimentation studies were conducted to explore S100A4 oligomerization and whether the C-terminal tail mediates self-association. The weight-average molecular masses of Ca^{2+}-bound S100A4, apo-S100A4, and Ca^{2+}-bound Δ13C S100A4 are 37429 ± 2843, 26710 ± 2773, and 21969 ± 1989 Da, respectively (Figure 10). The masses of S100A4 and Δ13C S100A4 dimers calculated from their sequences are 23194 and 19983 Da, respectively. The correspondence of the calculated and observed molecular

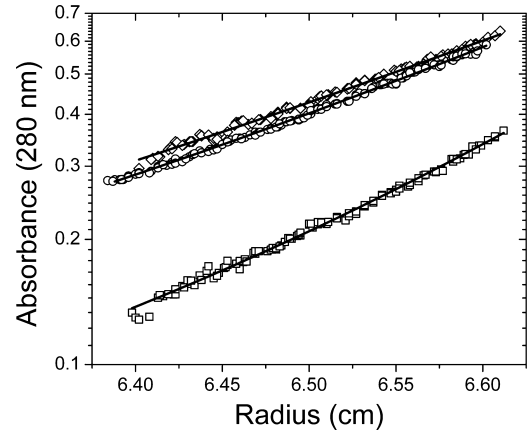

FIGURE 10: Sedimentation equilibrium measurements taken at 25 °C. The solid lines represent the best fit from a global nonlinear least-squares analysis of data obtained at 15000 and 22000 rpm: (□) 38 μM wild-type S100A4 and $CaCl_2$ (subunit concentration), (○) 54 μM wild-type S100A4 and EDTA/EGTA (subunit concentration), and (◇) 61 μM Δ13C S100A4 and $CaCl_2$ (subunit concentration).

mass of Ca^{2+}-bound Δ13C S100A4 shows that it is dimeric at these protein concentrations. This conclusion was confirmed by sedimentation velocity analysis conducted as a function of Δ13C S100A4 concentration. $S_{20,w}$ linearly decreases with an increase in Δ13C S100A4 concentration as expected for a stable oligomer (data not shown).

In contrast, both apo and Ca^{2+}-bound S100A4 dimers oligomerize to higher-order aggregates and Ca^{2+} facilitates this process. A dimer−tetramer reaction is the simplest association model that fits the data. K_d values of 19.84 (7.85, 41.27) and 469.4 (194.20, 1910.48) μM were resolved for Ca^{2+}-bound and apo-S100A4, respectively. These results were confirmed by sedimentation velocity analysis. $S_{20,w}$ linearly increases with an increase in S100A4 concentration (more so for the Ca^{2+}-bound protein) as expected for a self-association reaction (data not shown). These observations indicate that the C-terminal tail mediates oligomerization of the Ca^{2+}-S100A4 dimer at high protein concentrations.

Binding of Myosin-IIA to Ca^{2+}-S100A4. Next we examined S100A4 binding to peptides derived from the C-terminal coiled-coil domain of myosin-IIA that are monomeric and do not polymerize into filaments under any ionic strength. As found previously for myosin-IIA rods ($MIIA^{1338-1960}$) (*29*), no interaction is observed between S100A4 and $MIIA^{1908-1923}$, $MIIA^{1893-1923}$, or $MIIA^{1851-1960}$ in the absence of Ca^{2+}, even at peptide and protein concentrations as high as 10^{-3} M for $MIIA^{1908-1923}$ and $MIIA^{1893-1923}$. However, when Ca^{2+} is present, all of the constructs derived from the C-terminus of myosin-IIA bind S100A4 with relatively high affinity at either a low or physiological salt levels (Figure 11A,B and Table 6), confirming the Ca^{2+} dependence of the S100A4−MIIA interaction. For $MIIA^{1908-1923}$, which comprises the minimal S100A4 binding site, the affinity is slightly higher (K_d = 0.89 ± 0.12 μM) than for filamentous myosin-IIA rods ($MIIA^{1338-1960}$; K_d = 2.7 ± 0.6 μM) under low-salt conditions (20 mM KCl). Similarly under low-salt conditions, Ca^{2+}-S100A4 binds $MIIA^{1893-1923}$ and $MIIA^{1851-1960}$ with 6−8-fold higher affinities than filamentous rods ($MIIA^{1338-1960}$). Together, these data indicate that Ca^{2+}-S100A4 binds to monomeric MIIA constructs more tightly than to polymeric MIIA rods. It should be noted that these comparisons were made

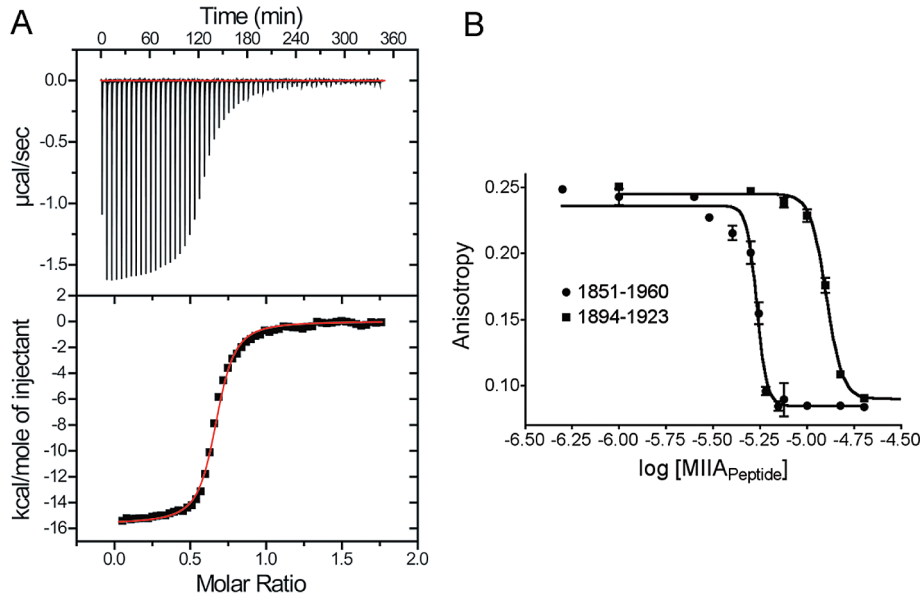

FIGURE 11: Thermodynamic data showing MIIA peptide binding to S100A4. (A) Isothermal titration calorimetry (ITC) of MIIA$^{1893-1923}$ peptide (low salt; $n = 1$). (B) Competition fluorescence anisotropy of MIIA$^{1893-1923}$ and MIIA$^{1851-1960}$ at a physiological salt concentration.

Table 6: Dissociation Constants for MIIA Binding to S100A4

MIIA construct	K_d (μM)
S100A4 + MIIA$^{1338-1960}$ (rod, low salt)	2.7 ± 0.6^a
S100A4 + MIIA$^{1851-1960}$ (coiled coil + tailpiece, low salt)	0.41 ± 0.01^b
S100A4 + MIIA$^{1851-1960}$ (coiled coil + tailpiece, high salt)	0.50 ± 0.01^b
S100A4 + MIIA$^{1893-1923}$ (coiled coil, low salt)	0.34 ± 0.02^c
S100A4 + MIIA$^{1893-1923}$ (coiled coil, high salt)	1.1 ± 0.1^d
S100A4 + MIIA$^{1908-1923}$ (minimal S100A4 site, low salt)	0.50 ± 0.20^e
S100A4 + MIIA$^{1908-1923}$ (minimal S100A4 site, low salt)	0.89 ± 0.12^f
S100A4 + MIIA$^{1908-1923}$ (minimal S100A4 site, high salt)	1.7 ± 0.2^f

[a] This value is from published studies (*29*). The dissociation constant for the Ca^{2+}-dependent interaction between S100A4 and MIIA rod filaments was determined in a cosedimentation assay under low-salt conditions [20 mM Tris (pH 7.5), 20 mM NaCl, 2 mM $MgCl_2$, 0.3 mM $CaCl_2$, 1 mM DTT, 0.02% NaN_3]. Binding could not be examined under high-salt conditions (150 mM KCl) since S100A4 disassembles the MIIA rods under these conditions. [b] The dissociation constant for the Ca^{2+}-dependent interaction between S100A4 and MIIA$^{1851-1960}$ was determined in competition studies with fluorescently labeled MIIA$^{1908-1923}$ using a fluorescence polarization assay under low- and high-salt conditions [20 mM Tris (pH 7.5), 20 or 150 mM KCl, 1 mM DTT, 0.02% NaN_3, and 0.5 mM $CaCl_2$]. MIIA$^{1851-1960}$ comprises part of the coiled-coil domain and the C-terminal tailpiece of MIIA. [c] The dissociation constant for the Ca^{2+}-dependent interaction between S100A4 and MIIA$^{1893-1923}$ was determined using ITC under low-salt conditions [20 mM Tris (pH 7.5), 20 mM KCl, 250 μM TCEP, and 0.8 mM $CaCl_2$]. MIIA$^{1893-1923}$ comprises part of the coiled-coil domain of MIIA. [d] The dissociation constant for the Ca^{2+}-dependent interaction between S100A4 and MIIA$^{1893-1923}$ was determined in competition studies with fluorescently labeled MIIA$^{1908-1923}$ using a fluorescence polarization assay under high-salt conditions [20 mM Tris (pH 7.5), 150 mM KCl, 1 mM DTT, 0.02% NaN_3, and 0.5 mM $CaCl_2$]. [e] The dissociation constant for the Ca^{2+}-dependent interaction between S100A4 and MIIA$^{1908-1923}$ was determined using ITC under low-salt conditions [20 mM Tris (pH 7.5), 20 mM KCl, 250 μM TCEP, and 0.8 mM $CaCl_2$]. MIIA$^{1908-1923}$ comprises a portion of the coiled-coil domain of MIIA but is not predicted to form a coiled coil. [f] The dissociation constant for the Ca^{2+}-dependent interaction between S100A4 and FITC-MIIA$^{1908-1923}$ was determined as described previously using a fluorescence polarization assay (*71*) under low- or high-salt conditions [20 mM Tris (pH 7.5), 20 or 15 mM KCl, 1 mM DTT, 0.02% NaN_3, and 0.5 mM $CaCl_2$].

under low-salt conditions because S100A4 depolymerizes MIIA rods under physiological conditions (150 mM KCl) (*29*).

We also examined binding of the MIIA peptides under physiological conditions (150 mM KCl) (Table 6). Specifically, Ca^{2+}-S100A4 binds the largest of these MIIA constructs, MIIA$^{1851-1960}$, with slightly higher affinity ($K_d = 0.50 \pm 0.01$ μM) than the smaller MIIA$^{1893-1923}$ ($K_d = 1.1 \pm 0.1$ μM) and MIIA$^{1908-1923}$ ($K_d = 1.7 \pm 0.2$ μM) peptides. The shorter peptides exhibit some salt dependence in their binding to S100A4, whereas salt concentration has no discernible effect on the binding of the larger peptide (MIIA$^{1851-1960}$) (Table 6). Notably, these studies demonstrate that MIIA does not have to be in a filament or in a coiled-coil conformation to bind Ca^{2+}-loaded S100A4.

Mapping the Myosin-IIA Binding Site on Ca^{2+}-S100A4. A comparison of apo and Ca^{2+}-bound S100A4 shows that there is a large rearrangement in the position of helix 3, which exposes a hydrophobic pocket on Ca^{2+}-S100A4 that is not accessible in apo-S100A4 (*23*) (Figure 4A). A similar Ca^{2+}-dependent conformational change is required for other S100 proteins to bind their respective targets (*34–36, 82–84*). Therefore, we used NMR spectroscopic methods to investigate the binding of MIIA$^{1908-1923}$ to Ca^{2+}-S100A4 to determine whether this pocket comprises the MIIA binding site.

During the titration of the MIIA$^{1908-1923}$ peptide into Ca^{2+}-S100A4, many of the resonances broadened and in some cases disappeared or reappeared, consistent with MIIA$^{1908-1923}$ binding; however, all of the observable correlations could be assigned sequence specifically when the titration was complete (Figure 12). An analysis of chemical shifts, NOE correlations, and hydrogen exchange data (*85, 86*) demonstrates that very few changes in the secondary structure of Ca^{2+}-bound S100A4 are observed upon binding of MIIA$^{1908-1923}$ (data not shown). Thus, the chemical shift perturbation data could be used reliably to map the MIIA$^{1908-1923}$ peptide binding site on Ca^{2+}-S100A4. Unlike the transition from apo-S100A4 to holo-S100A4, in which nearly two-thirds of the resonances undergo large changes in chemical shift (Figure 13A), MIIA$^{1908-1923}$ binding produces chemical shift perturbations smaller in magnitude. Following peptide addition, perturbations of amide ^1H, ^{15}N, $^{13}C_\alpha$, and $^{13}C_\beta$ resonances (>75 Hz total per residue) occur for residues in helix 1 (Val11, Met12, Ser14, and Phe16), the pseudo-EF-hand (Ser20, Phe27, Lys28, and Asn30), the hinge (Glu41, Gly47,

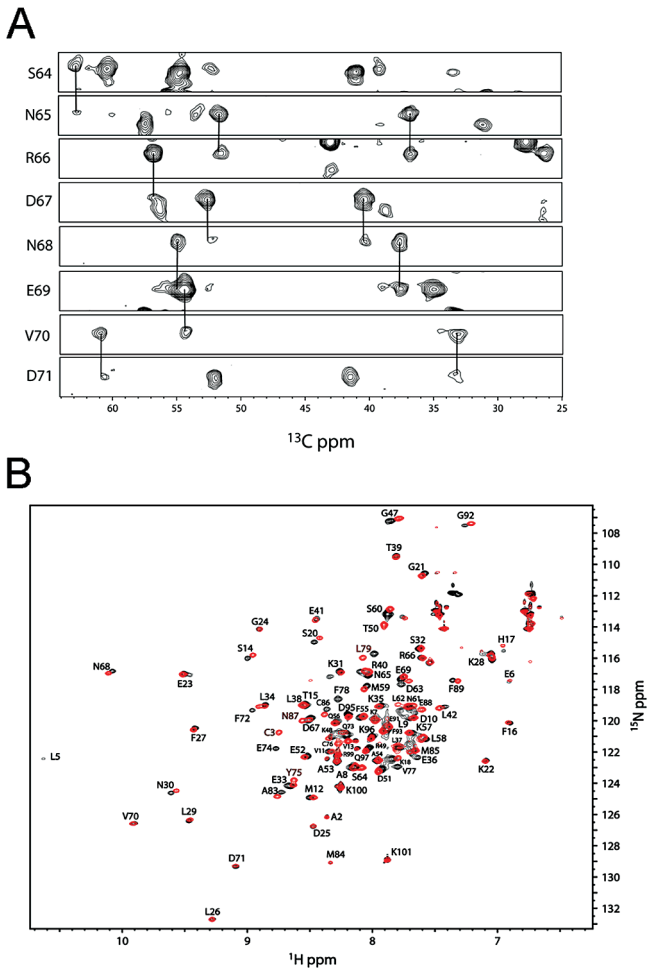

FIGURE 12: Nuclear magnetic resonance (NMR) data together with the resonance assignments for Ca^{2+}-S100A4 in the presence and absence of the MIIA$^{1908-1923}$ peptide. (A) Strips from ^{15}N planes of a three-dimensional HNCACB data set for ^{13}C- and ^{15}N-labeled S100A4 bound to the MIIA$^{1908-1923}$ peptide in the presence of Ca^{2+}, which illustrates the quality of the data used for making the resonance assignments. (B) Overlay of ^{1}H−^{15}N HSQC data for Ca^{2+}-S100A4 in the MIIA$^{1908-1923}$ peptide-bound (red contours) and free (black contours) states.

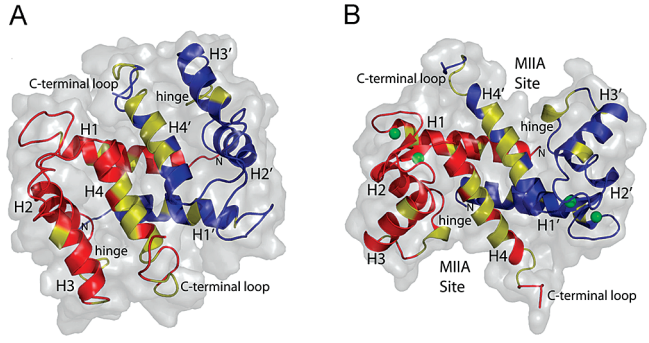

FIGURE 13: Ribbon and surface diagrams of S100A4 in the (A) apo and (B) Ca^{2+}-bound states. Residues colored yellow show significant chemical shift perturbations and exchange broadening effects upon binding of the MIIA$^{1908-1923}$ peptide.

Lys48, Thr50, and Asp51), helix 3 (Ser60 and Leu62), the typical EF-hand (Asn68 and Val70), helix 4 (Phe78, Leu79, Met85, and Cys86), and the C-terminal tail (Gly92) of Ca^{2+}-S100A4 when the MIIA$^{1908-1923}$ peptide is added (Figure 13B). The changes in chemical shift for these specific residues are consistent with MIIA$^{1908-1923}$ binding in a hydrophobic pocket of S100A4 that is exposed upon addition of Ca^{2+}.

DISCUSSION

Our biochemical studies demonstrate that in the presence of target (e.g., a myosin-IIA peptide), the Ca^{2+} binding affinity of S100A4 in both EF-hands increases by more than 1 order of magnitude (K_d values of 3.6 and 0.26 μM for the pseudo-EF-hand and typical EF-hand, respectively, in the presence of MIIA$^{1851-1960}$). These results with the human S100A4−MIIA complex are similar to observations with other S100 proteins (*82, 87–89*) and demonstrate that like other Ca^{2+}-binding proteins (e.g., calmodulin) (*90*), S100 protein family members exhibit a higher affinity for Ca^{2+} in the presence of their target proteins. Target-induced tuning of Ca^{2+} affinities has important implications when considering S100 protein activation in vivo. Intracellular Ca^{2+} levels are tightly controlled, with quiescent cells exhibiting Ca^{2+} concentrations of ~100 nM; however, local Ca^{2+} levels can rapidly and transiently increase to low micromolar levels (*91–94*). Thus, the increased Ca^{2+} binding affinities exhibited by S100A4 in the presence of the myosin-IIA peptide could tune S100A4 activation and inactivation in response to specific temporal and spatial cellular events.

Similar to the case for other S100 family members, Ca^{2+} binding has a dramatic effect on S100A4 conformation. Superimposition of the apo-S100A4 NMR structure and the Ca^{2+}-bound S100A4 X-ray structure presented here reveals a large-scale rearrangement of the hinge region and helix 3. In apo-S100A4, helices 3 and 4 adopt a nearly antiparallel orientation relative to each other (helical angle of 162 ± 4°), and this conformation is stabilized by multiple interactions between helix 3 and helices 2 and 4. In contrast, in the Ca^{2+}-bound S100A4 structure, the EF-hands change their conformation due to metal binding, which causes helix 2 and helix 3 to rotate relative to the almost immobile core formed by helices 1 and 4. In the Ca^{2+}- S100A4 structure, helix 3 is nearly orthogonal to helix 2 and helix 4 (helical angles of 102 ± 2° and 107 ± 2°, respectively). This reorganization results in the formation of a cleft between helices 3 and 4 that is appropriately configured to accept target peptides such as those from myosin-IIA. The largest conformational transition occurs in the hinge region that together with helices 3 and 4 contributes to the target binding pocket.

Structural comparisons indicate that Ca^{2+} activation brings about similar conformational changes in S100A4, S100A1, S100A6, S100A11, S100A12, S100A13, and S100B in terms of overall structure and interhelical angles (*23, 34, 35, 75–78, 95–99*). Helices 1 and 4, which are locked in the dimer interface, are the most structurally conserved in both the apo and Ca^{2+}-bound forms. Helices 2 and 3 and especially the hinge region deviate most among both apo and Ca^{2+}-bound structures. Thus, conformational variability within the target binding pocket is likely to be important for target protein specificity within the S100 family.

The C-terminal tail is the most flexible region in all S100 structures, as the observed conformations and orientations vary considerably in the structures listed in Table 3. On the basis of crystal lattice interactions, the current S100A4

structure suggests interdimer self-association. Interestingly, in the holmium-substituted S100A7 structure (*100*), the C-terminal tail self-associates with the binding pocket of the same S100 subunit via intramolecular interactions. The position of the peptide within the pocket is quite similar to that in S100A4; however, its contacts within the pocket and especially the structure of the hinge region are distinct.

To determine whether intermolecular interactions between S100A4 dimers can occur in solution, a 13mer peptide derived from the C-terminal tail of S100A4 (residues Pro98−Lys101) was titrated into dimeric Ca^{2+}-S100A4. Although perturbations in both ^{1}H and ^{15}N backbone resonances in Ca^{2+}-S100A4 were detected in the hinge region and helix 4 and are consistent with interdimer interactions observed in the X-ray structure, the affinity of this peptide is quite low for binding intact Ca^{2+}-S100A4 ($K_d = 1.05 \pm 0.10$ mM). However, sedimentation equilibrium studies indicate that at high S100A4 concentrations, full-length S100A4 can self-associate into tetramers in a Ca^{2+}-dependent manner. Moreover, assembly is mediated by the C-terminal tail as deletion of these residues results in the formation of a stable dimer. Notably, in normal and tumor cells, S100A4 dimer concentrations range from 3 to 5 μM, with concentrations as high as 10 μM in some carcinoma cells (*33*) (unpublished observations). Given the magnitudes of the equilibrium constants governing formation of S100A4 tetramers, intracellular S100A4 is likely to be predominantly a dimer.

It is also notable that the structure of S100A4 crystallized in the presence of Ca^{2+} and PCP shows no indication of bound PCP; however, crystals could be obtained only in the presence of PCP. We propose that inhibitor binding in solution promotes an open conformation similar to those observed in other ternary S100 complexes (*84, 101, 102*) and that the inhibitor exchanges for the C-terminal tail of the nascent S100A4 molecule, thus facilitating crystallization.

As with other S100 proteins, the interaction between S100A4 and the C-terminus of myosin-IIA is dependent on a "Ca^{2+}-switch" mechanism for binding. Our NMR studies demonstrate that the $MIIA^{1908-1923}$ peptide binds in a Ca^{2+}-induced hydrophobic pocket of S100A4 that is comprised of residues in the hinge region, helix 3, and helix 4. These findings are consistent with other S100−target peptide complexes, including S100B−p53, S100B−NDR, S100B−TRTK, S100A10−annexin II, and S100A11−annexin I complexes (*82, 84, 88, 96, 101, 103*); however, when compared among the S100 proteins, the residues comprising the pocket are not conserved. The low degree of sequence conservation between S100 homologues within the binding pocket suggests that this sequence divergence may provide a mechanism for target specific recognition and binding (*104*).

These studies demonstrate that S100A4 binds with high affinity to short MIIA peptides (e.g., $MIIA^{1908-1923}$) and MIIA peptides that are predicted to form a coiled coil (e.g., $MIIA^{1893-1923}$ and $MIIA^{1851-1960}$). Notably, a highly conserved 29-residue sequence, termed the assembly competence domain or ACD, was identified as a critical region for myosin-II assembly (*30, 31*). The ACD and the sequences immediately flanking it have been termed the extended ACD (residues 1857−1919 in myosin-IIA) and are predicted to form a very stable coiled coil (*30*). Our previous studies demonstrate that the S100A4 binding site (residues 1908−1923) maps to the C-terminal end of the extended ACD on myosin-IIA (*29*). It is also important to note that nearly all S100−target complexes examined thus far show that each subunit in a S100 dimer binds to a single helical peptide (*84, 101, 102*). On the basis of these observations, we propose that S100A4 promotes myosin-IIA filament disassembly by binding a single polypeptide chain of the coiled coil. This would allow for Ca^{2+}-dependent conformational rearrangements that may result in partial unwinding of the coiled coil.

ACKNOWLEDGMENT

We thank Dr. Michael Brenowitz for assistance with analytical ultracentrifugation experiments and the staff of the X6A beamline at the National Synchrotron Light Source for the help. We acknowledge support from the Albert Einstein College of Medicine Cancer Center (National Cancer Institute Grant P30CA13330).

REFERENCES

1. Donato, R. (2001) S100: A multigenic family of calcium-modulated proteins of the EF-hand type with intracellular and extracellular functional roles. *Int. J. Biochem. Cell Biol. 33*, 637–668.
2. Marenholz, I., Heizmann, C. W., and Fritz, G. (2004) S100 proteins in mouse and man: From evolution to function and pathology (including an update of the nomenclature). *Biochem. Biophys. Res. Commun. 322*, 1111–1122.
3. Zimmer, D. B., Cornwall, E. H., Landar, A., and Song, W. (1995) The S100 protein family: History, function, and expression. *Brain Res. Bull. 37*, 417–429.
4. Santamaria-Kisiel, L., Rintala-Dempsey, A. C., and Shaw, G. S. (2006) Calcium-dependent and -independent interactions of the S100 protein family. *Biochem. J. 396*, 201–214.
5. Grigorian, M. S., Tulchinsky, E. M., Zain, S., Ebralidze, A. K., Kramerov, D. A., Kriajevska, M. V., Georgiev, G. P., and Lukanidin, E. M. (1993) The mts1 gene and control of tumor metastasis. *Gene 135*, 229–238.
6. Takenaga, K., Nakamura, Y., and Sakiyama, S. (1994) Cellular localization of pEL98 protein, an S100-related calcium binding protein, in fibroblasts and its tissue distribution analyzed by monoclonal antibodies. *Cell Struct. Funct. 19*, 133–141.
7. Helfman, D. M., Kim, E. J., Lukanidin, E., and Grigorian, M. (2005) The metastasis associated protein S100A4: Role in tumour progression and metastasis. *Br. J. Cancer 92*, 1955–1958.
8. Garrett, S. C., Varney, K. M., Weber, D. J., and Bresnick, A. R. (2006) S100A4, a mediator of metastasis. *J. Biol. Chem. 281*, 677–680.
9. Rudland, P. S., Platt-Higgins, A., Renshaw, C., West, C. R., Winstanley, J. H., Robertson, L., and Barraclough, R. (2000) Prognostic significance of the metastasis-inducing protein S100A4 (p9Ka) in human breast cancer. *Cancer Res. 60*, 1595–1603.
10. Gongoll, S., Peters, G., Mengel, M., Piso, P., Klempnauer, J., Kreipe, H., and von Wasielewski, R. (2002) Prognostic significance of calcium-binding protein S100A4 in colorectal cancer. *Gastroenterology 123*, 1478–1484.
11. Davies, B. R., O'Donnell, M., Durkan, G. C., Rudland, P. S., Barraclough, R., Neal, D. E., and Mellon, J. K. (2002) Expression of S100A4 protein is associated with metastasis and reduced survival in human bladder cancer. *J. Pathol. 196*, 292–299.
12. Ninomiya, I., Ohta, T., Fushida, S., Endo, Y., Hashimoto, T., Yagi, M., Fujimura, T., Nishimura, G., Tani, T., Shimizu, K., Yonemura, Y., Heizmann, C. W., Schafer, B. W., Sasaki, T., and Miwa, K. (2001) Increased expression of S100A4 and its prognostic significance in esophageal squamous cell carcinoma. *Int. J. Oncol. 18*, 715–720.
13. Kimura, K., Endo, Y., Yonemura, Y., Heizmann, C. W., Schafer, B. W., Watanabe, Y., and Sasaki, T. (2000) Clinical significance of S100A4 and E-cadherin-related adhesion molecules in non-small cell lung cancer. *Int. J. Oncol. 16*, 1125–1131.
14. Cho, Y. G., Nam, S. W., Kim, T. Y., Kim, Y. S., Kim, C. J., Park, J. Y., Lee, J. H., Kim, H. S., Lee, J. W., Park, C. H., Song,

Y. H., Lee, S. H., Yoo, N. J., Lee, J. Y., and Park, W. S. (2003) Overexpression of S100A4 is closely related to the aggressiveness of gastric cancer. *APMIS 111*, 539–545.
15. Hernan, R., Fasheh, R., Calabrese, C., Frank, A. J., Maclean, K. H., Allard, D., Barraclough, R., and Gilbertson, R. J. (2003) ERBB2 up-regulates S100A4 and several other prometastatic genes in medulloblastoma. *Cancer Res. 63*, 140–148.
16. Rosty, C., Ueki, T., Argani, P., Jansen, M., Yeo, C. J., Cameron, J. L., Hruban, R. H., and Goggins, M. (2002) Overexpression of S100A4 in pancreatic ductal adenocarcinomas is associated with poor differentiation and DNA hypomethylation. *Am. J. Pathol. 160*, 45–50.
17. Saleem, M., Adhami, V. M., Ahmad, N., Gupta, S., and Mukhtar, H. (2005) Prognostic significance of metastasis-associated protein S100A4 (Mts1) in prostate cancer progression and chemoprevention regimens in an autochthonous mouse model. *Clin. Cancer Res. 11*, 147–153.
18. Zou, M., Al-Baradie, R. S., Al-Hindi, H., Farid, N. R., and Shi, Y. (2005) S100A4 (Mts1) gene overexpression is associated with invasion and metastasis of papillary thyroid carcinoma. *Br. J. Cancer 93*, 1277–1284.
19. Stein, U., Arlt, F., Walther, W., Smith, J., Waldman, T., Harris, E. D., Mertins, S. D., Heizmann, C. W., Allard, D., Birchmeier, W., Schlag, P. M., and Shoemaker, R. H. (2006) The metastasis-associated gene S100A4 is a novel target of β-catenin/T-cell factor signaling in colon cancer. *Gastroenterology 131*, 1486–1500.
20. Fearon, E. R., and Vogelstein, B. (1990) A genetic model for colorectal tumorigenesis. *Cell 61*, 759–767.
21. Bienz, M., and Clevers, H. (2000) Linking colorectal cancer to Wnt signaling. *Cell 103*, 311–320.
22. Polakis, P. (2007) The many ways of Wnt in cancer. *Curr. Opin. Genet. Dev. 17*, 45–51.
23. Vallely, K. M., Rustandi, R. R., Ellis, K. C., Varlamova, O., Bresnick, A. R., and Weber, D. J. (2002) Solution structure of human mts1 (S100A4) as determined by NMR spectroscopy. *Biochemistry 41*, 12670–12680.
24. Kriajevska, M. V., Cardenas, M. N., Grigorian, M. S., Ambartsumian, N. S., Georgiev, G. P., and Lukanidin, E. M. (1994) Non-muscle myosin heavy chain as a possible target for protein encoded by metastasis-related mts-1 gene. *J. Biol. Chem. 269*, 19679–19682.
25. Ford, H. L., Silver, D. L., Kachar, B., Sellers, J. R., and Zain, S. B. (1997) Effect of Mts1 on the structure and activity of nonmuscle myosin II. *Biochemistry 36*, 16321–16327.
26. Takenaga, K., Nakamura, Y., Sakiyama, S., Hasegawa, Y., Sato, K., and Endo, H. (1994) Binding of pEL98 protein, an S100-related calcium-binding protein, to nonmuscle tropomyosin. *J. Cell Biol. 124*, 757–768.
27. Watanabe, Y., Usada, N., Minami, H., Morita, T., Tsugane, S., Ishikawa, R., Kohama, K., Tomida, Y., and Hidaka, H. (1993) Calvasculin, as a factor affecting the microfilament assemblies in rat fibroblasts transfected by src gene. *FEBS Lett. 324*, 51–55.
28. Kriajevska, M., Fischer-Larsen, M., Moertz, E., Vorm, O., Tulchinsky, E., Grigorian, M., Ambartsumian, N., and Lukanidin, E. (2002) Liprin β1, a member of the family of LAR transmembrane tyrosine phosphatase-interacting proteins, is a new target for the metastasis-associated protein S100A4 (Mts1). *J. Biol. Chem. 277*, 5229–5235.
29. Li, Z. H., Spektor, A., Varlamova, O., and Bresnick, A. R. (2003) Mts1 regulates the assembly of nonmuscle myosin-IIA. *Biochemistry 42*, 14258–14266.
30. Sohn, R. L., Vikstrom, K. L., Strauss, M., Cohen, C., Szent-Gyorgyi, A. G., and Leinwand, L. A. (1997) A 29 residue region of the sarcomeric myosin rod is necessary for filament formation. *J. Mol. Biol. 266*, 317–330.
31. Cohen, C., and Parry, D. A. (1998) A conserved C-terminal assembly region in paramyosin and myosin rods. *J. Struct. Biol. 122*, 180–187.
32. Dulyaninova, N. G., Malashkevich, V. N., Almo, S. C., and Bresnick, A. R. (2005) Regulation of myosin-IIA assembly and Mts1 binding by heavy chain phosphorylation. *Biochemistry 44*, 6867–6876.
33. Li, Z. H., and Bresnick, A. R. (2006) The S100A4 metastasis factor regulates cellular motility via a direct interaction with myosin-IIA. *Cancer Res. 66*, 5173–5180.
34. Drohat, A. C., Baldisseri, D. M., Rustandi, R. R., and Weber, D. J. (1998) Solution structure of calcium-bound rat S100B($\beta\beta$) as determined by nuclear magnetic resonance spectroscopy. *Biochemistry 37*, 2729–2740.
35. Wright, N. T., Varney, K. M., Ellis, K. C., Markowitz, J., Gitti, R. K., Zimmer, D. B., and Weber, D. J. (2005) The three-dimensional solution structure of Ca^{2+}-bound S100A1 as determined by NMR spectroscopy. *J. Mol. Biol. 353*, 410–426.
36. Sastry, M., Ketchem, R. R., Crescenzi, O., Weber, C., Lubienski, M. J., Hidaka, H., and Chazin, W. J. (1998) The three-dimensional structure of Ca^{2+}-bound calcyclin: Implications for Ca^{2+}-signal transduction by S100 proteins. *Structure 6*, 223–231.
37. Otwinowski, W., and Minor, F. (1997) Processing of X-ray diffraction data collected in oscillation mode. *Methods Enzymol. 276*, 307–326.
38. Collaborative Computational Project Number 4 (1994) The CCP4 suite: Programs for protein crystallography. *Acta Crystallogr. D50*, 760–763.
39. Schneider, T. R., and Sheldrick, G. M. (2002) Substructure solution with SHELXD. *Acta Crystallogr. D58*, 1772–1779.
40. Sheldrick, G. M. (2002) Macromolecular phasing with SHELXE. *Z. Kristallogr. 217*, 644–650.
41. Lamzin, V. S., Perrakis, A., and Wilson, K. S. (2001) *International Tables for Crystallography: The ARP/WARP suite for automated construction and refinement of protein models*, Volume F: Crystallography of biological macromolecules, Kluwer Academic Publishers, Dordrecht, The Netherlands.
42. Emsley, P., and Cowtan, K. (2004) Coot: Model-building tools for molecular graphics. *Acta Crystallogr. D60*, 2126–2132.
43. Hooft, R. W., Vriend, G., Sander, C., and Abola, E. E. (1996) Errors in protein structures. *Nature 381*, 272.
44. Laskowski, R., MacArthur, M., Moss, D., and Thornton, J. (1993) PROCHECK: A program to check the stereochemical quality of protein structures. *J. Appl. Crystallogr. 26*, 283–291.
45. Krissinel, E., and Henrick, K. (2004) Secondary-structure matching (SSM), a new tool for fast protein structure alignment in three dimensions. *Acta Crystallogr. D60*, 2256–2268.
46. Holm, L., and Sander, C. (1996) Mapping the protein universe. *Science 273*, 595–603.
47. Holm, L., and Park, J. (2000) DaliLite workbench for protein structure comparison. *Bioinformatics 16*, 566–567.
48. Yap, K. L., Ames, J. B., Swindells, M. B., and Ikura, M. (2002) Vector geometry mapping. A method to characterize the conformation of helix-loop-helix calcium-binding proteins. *Methods Mol. Biol. 173*, 317–324.
49. Marion, D., Ikura, M., Tschudin, R., and Bax, A. (1989) Rapid recording of 2d NMR-spectra without phase cycling: Application to the study of hydrogen-exchange in proteins. *J. Magn. Reson. 85*, 393–399.
50. Delaglio, F., Grzesiek, S., Vuister, G. W., Zhu, G., Pfeifer, J., and Bax, A. (1995) NMRPipe: A multidimensional spectral processing system based on UNIX pipes. *J. Biomol. NMR 6*, 277–293.
51. Zhu, G. A., and Bax, A. (1992) 2-Dimensional linear prediction for signals truncated in both dimensions. *J. Magn. Reson. 98*, 192–199.
52. Zhu, G., and Bax, A. (1990) Improved linear prediction for truncated signals of known phase. *J. Magn. Reson. 90*, 405–410.
53. Live, D. H., Davis, D., Agosta, W., and Cowburn, D. (1984) Long range hydrogen bond mediated effects in peptides: Nitrogen-15 NMR study of gramicidin S in water and organic solvents. *J. Am. Chem. Soc. 106*, 1939–1941.
54. Spera, S., and Bax, A. (1991) Empirical correlation between protein backbone conformation and C-α and C-β C-13 nuclear-magnetic-resonance chemical-shifts. *J. Am. Chem. Soc. 113*, 5490–5492.
55. Edison, A. S., Abildgaard, F., Westler, W. M., Mooberry, E. S., and Markley, J. L. (1994) Practical introduction to theory and implementation of multinuclear, multidimensional nuclear magnetic resonance experiments. *Methods Enzymol. 239*, 3–79.
56. Mori, S., Abeygunawardana, C., Johnson, M. O., and van Zijl, P. C. (1995) Improved sensitivity of HSQC spectra of exchanging protons at short interscan delays using a new fast HSQC (FHSQC) detection scheme that avoids water saturation. *J. Magn. Reson., Ser. B 108*, 94–98.
57. Kay, L., Marion, D., and Bax, A. (1989) *J. Magn. Reson. 84*, 72–84.
58. Bax, A., and Davis, D. (1985) *J. Magn. Reson. 65*, 355–360.
59. Cavanagh, J., and Rance, M. (1992) Suppression of cross-relaxation effects in Tocsy spectra via a modified dipsi-2 mixing sequence. *J. Magn. Reson. 96*, 670–678.
60. Ikura, M., Bax, A., Clore, G. M., and Gronenborn, A. M. (1990) Detection of nuclear overhauser effects between degenerate amide

proton resonances by heteronuclear 3-dimensional nuclear-magnetic-resonance spectroscopy. *J. Am. Chem. Soc. 112*, 9020–9022.
61. Grzesiek, S., and Bax, A. (1992) An efficient experiment for sequential backbone assignment of medium-sized isotopically enriched proteins. *J. Magn. Reson. 99*, 201–207.
62. Muhandiram, D. R., Xu, G. Y., and Kay, L. E. (1993) An enhanced-sensitivity pure absorption gradient 4d N-15, C-13-edited noesy experiment. *J. Biomol. NMR 3*, 463–470.
63. Wittekind, M., and Mueller, L. (1993) Hncacb, a high-sensitivity 3d NMR experiment to correlate amide-proton and nitrogen resonances with the α-carbon and β-carbon resonances in proteins. *J. Magn. Reson., Ser. B 101*, 201–205.
64. Grzesiek, S., and Bax, A. (1992) Improved 3d triple-resonance NMR techniques applied to a 31-kDa protein. *J. Magn. Reson. 96*, 432–440.
65. Yamazaki, T., Lee, W., Revington, M., Mattiello, D. L., Dahlquist, F. W., Arrowsmith, C. H., and Kay, L. E. (1994) An Hnca pulse scheme for the backbone assignment of N-15,C-13,H-2-labeled proteins: Application to a 37-kDa Trp repressor DNA complex. *J. Am. Chem. Soc. 116*, 6464–6465.
66. Bax, A., and Pochapsky, S. S. (1992) Optimized recording of heteronuclear multidimensional NMR-spectra using pulsed field gradients. *J. Magn. Reson. 99*, 638–643.
67. Linse, S. (2002) Calcium binding to proteins studied via competition with chromophoric chelators. *Methods Mol. Biol. 173*, 15–24.
68. Andre, I., and Linse, S. (2002) Measurement of Ca^{2+}-binding constants of proteins and presentation of the CaLigator software. *Anal. Biochem. 305*, 195–205.
69. Philo, J. S. (2006) Improved methods for fitting sedimentation coefficient distributions derived by time-derivative techniques. *Anal. Biochem. 354*, 238–246.
70. Dukhanina, E. A., Dukhanin, A. S., Lomonosov, M. Y., Lukanidin, E. M., and Georgiev, G. P. (1997) Spectral studies on the calcium-binding properties of Mts1 protein and its interaction with target protein. *FEBS Lett. 410*, 403–406.
71. Garrett, S. C., Hodgson, L., Rybin, A., Toutchkine, A., Hahn, K. M., Lawrence, D. S., and Bresnick, A. R. (2008) A biosensor of S100A4 metastasis factor activation: Inhibitor screening and cellular activation dynamics. *Biochemistry 47*, 986–996.
72. Gibbs, F. E., Wilkinson, M. C., Rudland, P. S., and Barraclough, R. (1994) Interactions in vitro of p9Ka, the rat S-100-related, metastasis-inducing, calcium-binding protein. *J. Biol. Chem. 269*, 18992–18999.
73. Pedrocchi, M., Schafer, B. W., Durussel, I., Cox, J. A., and Heizmann, C. W. (1994) Purification and characterization of the recombinant human calcium-binding S100 proteins CAPL and CACY. *Biochemistry 33*, 6732–6738.
74. Dutta, K., Cox, C. J., Huang, H., Basavappa, R., and Pascal, S. M. (2002) Calcium coordination studies of the metastatic Mts1 protein. *Biochemistry 41*, 4239–4245.
75. Maler, L., Potts, B. C., and Chazin, W. J. (1999) High resolution solution structure of apo calcyclin and structural variations in the S100 family of calcium-binding proteins. *J. Biomol. NMR 13*, 233–247.
76. Otterbein, L. R., Kordowska, J., Witte-Hoffmann, C., Wang, C. L., and Dominguez, R. (2002) Crystal structures of S100A6 in the Ca^{2+}-free and Ca^{2+}-bound states: The calcium sensor mechanism of S100 proteins revealed at atomic resolution. *Structure 10*, 557–567.
77. Rustandi, R. R., Baldisseri, D. M., Inman, K. G., Nizner, P., Hamilton, S. M., Landar, A., Landar, A., Zimmer, D. B., and Weber, D. J. (2002) Three-dimensional solution structure of the calcium-signaling protein apo-S100A1 as determined by NMR. *Biochemistry 41*, 788–796.
78. Drohat, A. C., Amburgey, J. C., Abildgaard, F., Starich, M. R., Baldisseri, D., and Weber, D. J. (1996) Solution structure of rat apo-S100B($\beta\beta$) as determined by NMR spectroscopy. *Biochemistry 35*, 11577–11588.
79. Chaudhuri, D., Horrocks, W. D., Jr., Amburgey, J. C., and Weber, D. J. (1997) Characterization of lanthanide ion binding to the EF-hand protein S100β by luminescence spectroscopy. *Biochemistry 36*, 9674–9680.
80. Inman, K. G., Baldisseri, D. M., Miller, K. E., and Weber, D. J. (2001) Backbone dynamics of the calcium-signaling protein apo-S100B as determined by ^{15}N NMR relaxation. *Biochemistry 40*, 3439–3448.
81. Linse, S., Brodin, P., Johansson, C., Thulin, E., Grundstrom, T., and Forsen, S. (1988) The role of protein surface charges in ion binding. *Nature 335*, 651–652.
82. Rustandi, R. R., Drohat, A. C., Baldisseri, D. M., Wilder, P. T., and Weber, D. J. (1998) The Ca^{2+}-dependent interaction of S100B($\beta\beta$) with a peptide derived from p 53. *Biochemistry 37*, 1951–1960.
83. Weber, D. J., Rustandi, R., Carrier, F., and Zimmer, D. B. (2000) Interaction of dimeric S100B($\beta\beta$) with the tumor suppressor protein: A model for Ca-dependent S100-target protein interactions, in *Calcium: The molecular basis of calcium action in biology and medicine*, pp 469–487, Kluwer Academic Publishers, Dordrecht, The Netherlands.
84. Inman, K. G., Yang, R., Rustandi, R. R., Miller, K. E., Baldisseri, D. M., and Weber, D. J. (2002) Solution NMR structure of S100B bound to the high-affinity target peptide TRTK-12. *J. Mol. Biol. 324*, 1003–1014.
85. Wuthrich, K. (1986) *NMR of proteins and nucleic acids*, John Wiley, New York.
86. Wishart, D. S., and Sykes, B. D. (1994) The C-13 chemical-shift index: A simple method for the identification of protein secondary structure using C-13 chemical-shift data. *J. Biomol. NMR 4*, 171–180.
87. Kordowska, J., Stafford, W. F., and Wang, C. L. (1998) Ca^{2+} and Zn^{2+} bind to different sites and induce different conformational changes in human calcyclin. *Eur. J. Biochem. 253*, 57–66.
88. Rustandi, R. R., Baldisseri, D. M., Drohat, A. C., and Weber, D. J. (1999) Structural changes in the C-terminus of Ca^{2+}-bound rat S100B($\beta\beta$) upon binding to a peptide derived from the C-terminal regulatory domain of p 53. *Protein Sci. 8*, 1743–1751.
89. Markowitz, J., Rustandi, R. R., Varney, K. M., Wilder, P. T., Udan, R., Wu, S. L., Horrocks, W. D., and Weber, D. J. (2005) Calcium-binding properties of wild-type and EF-hand mutants of S100B in the presence and absence of a peptide derived from the C-terminal negative regulatory domain of p 53. *Biochemistry 44*, 7305–7314.
90. Peersen, O. B., Madsen, T. S., and Falke, J. J. (1997) Intermolecular tuning of calmodulin by target peptides and proteins: Differential effects on Ca^{2+} binding and implications for kinase activation. *Protein Sci. 6*, 794–807.
91. Lee, J., Ishihara, A., Oxford, G., Johnson, B., and Jacobson, K. (1999) Regulation of cell movement is mediated by stretch-activated calcium channels. *Nature 400*, 382–386.
92. Berridge, M. J., Lipp, P., and Bootman, M. D. (2000) The versatility and universality of calcium signalling. *Nat. Rev. Mol. Cell Biol. 1*, 11–21.
93. Kindzelskii, A. L., and Petty, H. R. (2003) Intracellular calcium waves accompany neutrophil polarization, formylmethionylleucylphenylalanine stimulation, and phagocytosis: A high speed microscopy study. *J. Immunol. 170*, 64–72.
94. Clapham, D. E. (2007) Calcium signaling. *Cell 131*, 1047–1058.
95. Dempsey, A. C., Walsh, M. P., and Shaw, G. S. (2003) Unmasking the annexin I interaction from the structure of Apo-S100A11. *Structure 11*, 887–897.
96. Rety, S., Osterloh, D., Arie, J. P., Tabaries, S., Seeman, J., Russo-Marie, F., Gerke, V., and Lewit-Bentley, A. (2000) Structural basis of the Ca^{2+}-dependent association between S100C (S100A11) and its target, the N-terminal part of annexin I. *Structure 8*, 175–184.
97. Arnesano, F., Banci, L., Bertini, I., Fantoni, A., Tenori, L., and Viezzoli, M. S. (2005) Structural interplay between calcium(II) and copper(II) binding to S100A13 protein. *Angew. Chem., Int. Ed. 44*, 6341–6344.
98. Li, M., Zhang, P. F., Pan, X. W., and Chang, W. R. (2007) Crystal structure study on human S100A13 at 2.0 Å resolution. *Biochem. Biophys. Res. Commun. 356*, 616–621.
99. Maler, L., Sastry, M., and Chazin, W. J. (2002) A structural basis for S100 protein specificity derived from comparative analysis of apo and Ca^{2+}-calcyclin. *J. Mol. Biol. 317*, 279–290.
100. Brodersen, D. E., Etzerodt, M., Madsen, P., Celis, J. E., Thogersen, H. C., Nyborg, J., and Kjeldgaard, M. (1998) EF-hands at atomic resolution: The structure of human psoriasin (S100A7) solved by MAD phasing. *Structure 6*, 477–489.
101. Rety, S., Sopkova, J., Renouard, M., Osterloh, D., Gerke, V., Tabaries, S., Russo-Marie, F., and Lewit-Bentley, A. (1999) The crystal structure of a complex of p11 with the annexin II N-terminal peptide. *Nat. Struct. Biol. 6*, 89–95.
102. Rustandi, R. R., Baldisseri, D. M., and Weber, D. J. (2000) Structure of the negative regulatory domain of p 53 bound to S100B($\beta\beta$). *Nat. Struct. Biol. 7*, 570–574.

103. Bhattacharya, S., Large, E., Heizmann, C. W., Hemmings, B., and Chazin, W. J. (2003) Structure of the Ca^{2+}/S100B/NDR kinase peptide complex: Insights into S100 target specificity and activation of the kinase. *Biochemistry 42*, 14416–14426.
104. Kligman, D., and Hilt, D. C. (1988) The S100 protein family. *Trends Biochem. Sci. 13*, 437–443.
105. Ishikawa, K., Nakagawa, A., Tanaka, I., Suzuki, M., and Nishihira, J. (2000) The structure of human MRP8, a member of the S100 calcium-binding protein family, by MAD phasing at 1.9 Å resolution. *Acta Crystallogr. D56*, 559–566.
106. Itou, H., Yao, M., Fujita, I., Watanabe, N., Suzuki, M., Nishihira, J., and Tanaka, I. (2002) The crystal structure of human MRP14 (S100A9), a Ca^{2+}-dependent regulator protein in inflammatory process. *J. Mol. Biol. 316*, 265–276.
107. Moroz, O. V., Antson, A. A., Murshudov, G. N., Maitland, N. J., Dodson, G. G., Wilson, K. S., Skibshoj, I., Lukanidin, E. M., and Bronstein, I. B. (2001) The three-dimensional structure of human S100A12. *Acta Crystallogr. D57*, 20–29.
108. Svensson, L. A., Thulin, E., and Forsen, S. (1992) Proline cis-trans isomers in calbindin D9k observed by X-ray crystallography. *J. Mol. Biol. 223*, 601–606.

BI702537S